Spectrochimica Acta Part B: Atomic Spectroscopy 176 (2021) 106045

Contents lists available at ScienceDirect

Spectrochimica Acta Part B: Atomic Spectroscopy

journal homepage: www.elsevier.com/locate/sab

Advances in Thomson scattering diagnostics of plasmas used for chemical analysis☆

Kevin Finch, Dong Zhang, Yue She, Aldo Hernandez, Gerardo Gamez *

Department of Chemistry and Biochemistry, Texas Tech University, Lubbock, TX 79409-41061, USA

ARTICLE INFO

Keywords:
Thomson scattering
Chemical analysis plasmas
Plasma diagnostics
Electron temperature
Electron number density

ABSTRACT

The use of plasmas for chemical analysis is prevalent and new sorts are continually being explored for potential applications in this field. However, the underlying mechanisms of characteristic processes that occur in plasmas are not completely understood. Free electrons drive chemical reactions, are essential to many plasma inherent processes, and are responsible for sustaining the discharge while governing the kinetic energy transfer between other species. Thomson scattering (TS) is a powerful plasma diagnostic technique for elucidating the fundamental electron parameters of number density, kinetic temperature, and energy distribution function. TS advantages include providing the direct, radially and temporally resolved probing of free electrons, with little-to-no perturbation of the plasma, with no prior assumptions of local thermodynamic equilibrium conditions, and simultaneous electron density/temperature measurements. The aim of this review is to provide a brief explanation of the TS theory and the experimental requirements, as well as highlight selected novel instrumentation advances and insights about chemical analysis plasmas discovered in the most recent TS publications, not previously covered in other reviews.

1. Introduction

Plasmas are currently one of the most commonly used optical emission/ion sources for chemical analysis and are inclusive to a wide variety of sample types [1–9]. Therefore, novel plasma geometries are being rapidly developed for the improvement of qualitative and quantitative chemical measurements. On the other hand, the underlying mechanisms of these new plasma geometries are poorly understood and even some of the plasmas that have been around for a while still have some fundamental aspects that need better insights. It is imperative to understand the spatiotemporal evolution of the plasma species and the corresponding fundamental parameters in order to rationally improve their analytical performance, rather than through trial-and-error approaches. The distribution of species is unique to each type of plasma geometry and method of formation, specifically relating to the differences in kinetic energy and number density. These in turn affect characteristic processes including excitation, ionization, sputtering, and ambipolar diffusion through a multitude of mechanisms, such as electron impact and radiative recombination [1,10,11].

One such plasma species of interest are free electrons. Free electrons play a critical role pertaining to the chemical and physical interactions within plasmas used for chemical analysis. They also affect many equilibria processes with one of the most important being successive ionization states of the plasma species [12–14]. The primary driving force of kinetic energy transfer is free electron interactions between sample, surface, and gas [11]. The mechanisms of energy transfer can be elucidated by studying the spatial and temporal behavior of the electron number density (n_e), temperature (T_e), and energy distribution function (EEDF) for a more inclusive picture into understudied plasma geometries.

1.1. Techniques for measuring electron parameters

There are several techniques commonly implemented for insight into the fundamental properties of plasmas used for chemical analysis [11,15–17]. Optical emission spectroscopy (OES) methods, such as Stark broadening or Boltzmann plots, are regularly used to extract n_e and T_e, given the relatively simple experimental setup requirements. However,

☆ This paper is dedicated to Paul Farnsworth, following his retirement, in recognition of his outstanding contributions to the fields of optical emission spectroscopy and mass spectrometry.

* Corresponding author.
E-mail address: gerardo.gamez@ttu.edu (G. Gamez).

https://doi.org/10.1016/j.sab.2020.106045
Received 14 November 2020; Accepted 30 November 2020
Available online 4 February 2021
0584-8547/© 2020 Elsevier B.V. All rights reserved.

OES techniques may suffer from self-absorption and offer only inherently integrated measurements along the line-of-sight (LOS) [18–20]. More complicated experimental setups are required if radially resolved information is to be obtained from the measurement, e.g. computer aided tomography [21]. On the other hand, image processing techniques, such as Abel's inversion (mathematic transformation) can be implemented to extricate radially resolved values from LOS integrated images [22–24]. Nevertheless, Abel's inversion inherently introduces error that may accumulate towards the center of the plasma (typically the most analytically useful region) and requires the assumption of a radial symmetry across the plume [22,23,25]. Furthermore, OES methods typically require an assumption that the plasma is in local thermodynamic equilibrium (LTE) to obtain n_e and T_e, which is not reasonable for many plasmas used for chemical analysis [26–31].

Conversely, Langmuir probes are frequently used as an alternative to OES for measuring plasma electron fundamental parameters [27,31–34]. Advantages of Langmuir probes include being more cost-effective than some OES components, providing spatial resolution limited only by the size of the probe, having better sensitivity than the methods previously mentioned, and being a relatively simple experimental procedure. The main drawbacks to this technique are the likely perturbation of the plasma by the probe, material deposition on the probe, temperature thresholds which can result in damage of the probe, and the complicated nature of data analysis [31,35].

1.2. Thomson scattering

A more reliable approach to measuring the fundamental plasma parameters is through laser-induced scattering techniques, such as Thomson scattering (TS) [15]. Thomson scattered radiation, produced by elastic interactions of photons with free electrons in the plasma, allows for the direct, highly resolved spatial, spectral, and temporal probing necessary to obtain electron maps and the electron energy distribution function (EEDF), without assuming LTE or performing mathematical transformations to obtain radially resolved values [10,17,36–39]. TS also offers the advantage of allowing the n_e and T_e to be measured simultaneously, without the compounding of error from one calculation to the next [40]. In addition, the instrumental requirements for TS allow complementary scattering techniques such as Raman or Rayleigh scattering to be implemented with minimal/no changes to the existing experimental setups [41,42]. Perturbation of the plasma can also be avoided by this technique if the laser intensity is strictly controlled, as will be discussed below. Nevertheless, the implementation of plasma diagnostics by TS follows a stringent set of experimental requirements, which often require specialized instrumentation to accurately probe the fundamental parameters of plasmas.

1.3. Aim of review

The aim of this review is to present how TS measurements have contributed to the better understanding of the underlying mechanisms in plasmas used for chemical analysis. Herein, a short overview of the theory, experimental requirements, advances in instrumentation, and selected applications (most recent and not previously reviewed) with various plasma types within the last couple of decades will be discussed.

2. Thomson scattering

2.1. Theory basics

When laser light is passed through a plasma, the individual species present will scatter a portion of the incident radiation. The measured scattered power per unit of wavelength $P^i_\lambda(\lambda)$ by an individual species i within a plasma is modeled by the given Eq. [43],

$$P^i_\lambda(\lambda) = P_0 n_i f \left(\frac{d\sigma_i}{d\Omega}\right) \Delta\Omega S^i_\lambda(\lambda) L \quad (1)$$

where P_0 is the incident laser power, n_i is the density of the particle i responsible for the scattering, f is a constant that is determined by the efficiency of the optics and the detector, $d\sigma_i/d\Omega$ is the differential cross-section of the scattering from a species i, L is the detection volume length along the laser line, $\Delta\Omega S^i_\lambda(\lambda)$ represents the spectral density of scattered photons on species i as a function of wavelength over a solid angle $\Delta\Omega$ (Fig. 1A).

Through the interaction with incident radiation, the elastic scattering of protons and electrons bound to heavy particles occurs, called Rayleigh scattering [43]. The Rayleigh differential cross-section is the largest, compared with the other types of scattering cross-sections, and is effectively due to the most abundant species in the plasma being neutral gas atoms (for the plasmas reviewed herein), defined by the expression [45],

$$\frac{d\sigma^R}{d\Omega} = \frac{16\pi^4 a^i}{\lambda_i^4}\left(1 - sin^2\theta cos^2\varphi\right) \quad (2)$$

where a^i is the specific gas species' i volume polarizability, λ_i is the incident laser wavelength, θ is the scattering collection angle (angle between the incident laser and the scattered wave), and φ is the angle between the polarization of the incident beam ($\vec{E_i}$) and the plane of scattering (Fig. 1A).

As previously mentioned, TS is the scattering of radiation, with no kinetic energy transfer, caused by oscillations of unbound charges interacting with an incident electromagnetic wave. Electrons are the main species probed by this technique since they have low masses in comparison with the other species present, therefore allowing them to quickly react to changes in the incident radiation's electric field. The total Thomson scattered differential cross-section $d\sigma^T/d\Omega$ is given by the Eq. [46],

$$\frac{d\sigma^T}{d\Omega} = r_e^2\left(1 - sin^2\theta cos^2\varphi\right) \quad (3)$$

where r_e is the classic electron radius (2.818×10^{-15} m). The frequency of scattered photons is noticeably Doppler shifted due to the motion of the free electrons with respect to the incident laser beam and the detector [47,48]. This movement is influenced by a micro-scale fluctuating electric field that is further excited through electron thermal motion. The modulating electron distribution that results can be decomposed via Fourier methods to define the distribution as a superposition of n_e plane waves with a characteristic frequency and directional vector $\vec{K_f}$ (Fig. 1A) [43]. When a narrow bandwidth source, most effectively a laser, is used to probe a small region of the plasma, the resulting spectrum is broadened around the source's center wavelength. The collected scattered light carries inherent spatially resolved information along the laser axis where the incident photons have interacted with plasma species at different radial positions. In addition, the collected scattered light also carries inherent temporally resolved information because it is only produced when the pulsed laser beam interacts with the plasma species. Therefore, time resolved information is obtained only during the time the laser light probes the plasma species and the temporal resolution is limited only by the laser pulse duration.

When the incident laser light having an electric wave vector $\vec{K_i}$ interacts with a group of fluctuating electrons as described previously, the light sees a sinusoidal grating formed by the n_e wave and diffraction of the incident light occurs in the direction of the scattering wave vector $\vec{K_s}$. Through Newton's third law, the conservation of momentum must occur and thus $\vec{K_s}$ can be defined as the resultant vector, after the addition of $\vec{K_i}$

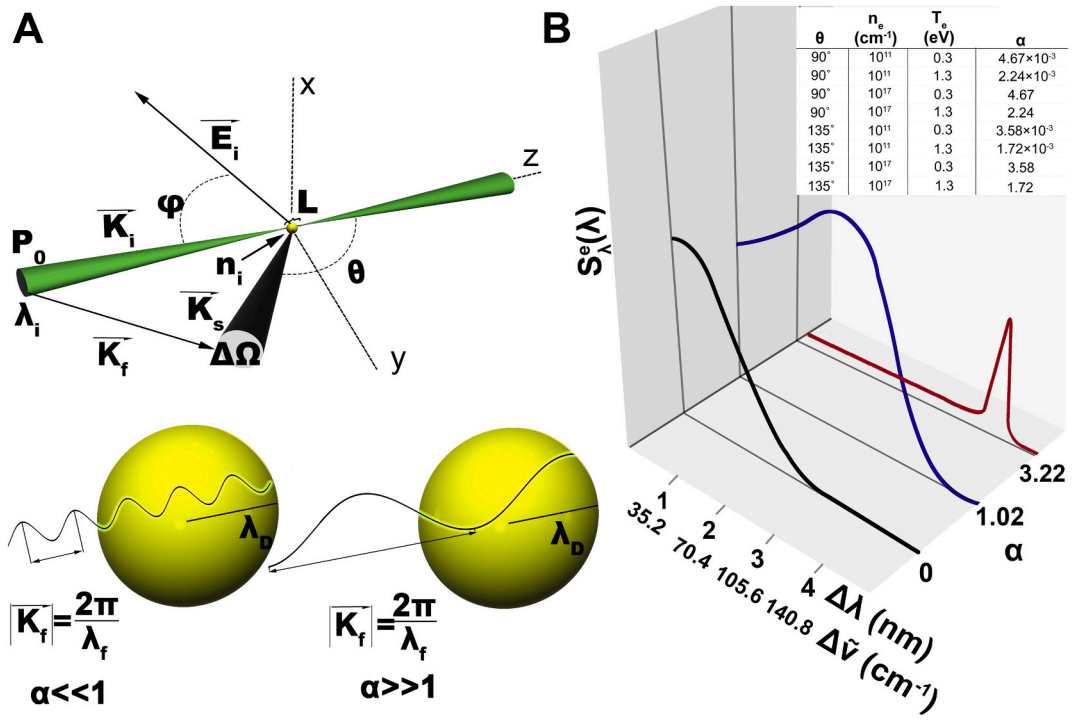

Fig. 1. (A) Shows the geometry of a typical TS experiment and the relationship of the Debye length (λ_D) to the scattering (Salpeter) parameter (α). (B) Example TS spectra, where the z-axis is the spectral density of scattered photons from the electron contribution ($S^e_\lambda(\lambda)$), shown for $\alpha \ll 1$ (incoherent), $\alpha \sim 1$ (transition range), $\alpha \gg 1$ (coherent) [44]. The corresponding table shows the effect of differences in scattering geometry, n_e, T_e, and the resulting α.

and $\vec{K}_f$ (Fig. 1A) [43]. Inside a Debye sphere, of which the volume is defined by the Debye length (λ_D), all electrons undergo coupled oscillations within the wavelength λ_f. Furthermore, the λ_f can be calculated from the magnitude of the vector as follows $|\vec{K}_f| = 2\pi/\lambda_f$ and its influence on the scattering (Salpeter) parameter α is shown in Fig. 1A [43]. Depending on the T_e and n_e of the plasma, laser wavelength, and the experimental geometry, laser light can be scattered coherently ($\lambda_f \gg \lambda_D$) or incoherently ($\lambda_f \ll \lambda_D$) which is defined by the scattering parameter α given by the relationship [49],

$$\alpha = \frac{\lambda_i}{4\pi sin\frac{\theta}{2}}\sqrt{\frac{4\pi n_e e^2}{k_B T_e}} \tag{4}$$

where e is the electron charge and k_B the Boltzmann constant. Coherently, also called collectively, scattered radiation stems from plasma waves of the electron (satellite peaks) and ion-acoustic (central portion) origin and is observed when $\alpha \gg 1$, however when incoherently scattered, the source is mostly from independent free electrons and is observed when $\alpha \ll 1$. In the transition range of $\sim 0.1 < \alpha < 1.5$ there are contributions from both coherent and incoherent scattering which greatly affect the shape of the scattered spectrum. The shape of the scattering spectrum reveals two satellite peaks symmetrically distributed in the frequency domain and centered at the laser's frequency, when the scattering is of a collective nature. Fig. 1B shows example TS spectra, of the electron contributions only, for different values of α and is further supplemented with a table at the top that shows a range of characteristic n_e and T_e for the plasmas described herein, and how α and λ_D change as a function of the angle θ. Furthermore, a narrow ion feature (nearly 2 orders-of-magnitude narrower than the electron contributions) is formed near the laser frequency, has a power that scales directly to the number density of ions squared (n^2_{ion}), and overlaps with the Rayleigh and stray-light signals. The n_e and T_e can be extracted by fitting the spectral density function without any need for calibration of the scattered power, assuming the EEDF follows a Maxwellian distribution [11,44]. The power of the satellite peaks scales directly to the $n_e/(1+\alpha^2)$ and the T_e, while the combined shape and distance from the laser central frequency is representative of both the T_e and n_e by the Salpeter approximation [11,44,46,49–51]. Coherent TS studies have less strict instrumental requirements (lower spectral resolution and contrast) to accurately probe the free electrons due to the satellite peaks' (scattered signal from the electron contribution) intensity being directly related to the n_e, their significantly greater frequency shifts, and the often much-higher n_e of the plasmas investigated. If the EEDF is of Maxwellian nature and the laser light is incoherently scattered, then a single Gaussian fit to the doubly Doppler shifted (red and blue shift) TS spectrum relates to the T_e by the equation [43],

$$T_e = \left(\frac{m_e c^2}{8k_B\lambda_i^2 sin^2\frac{\theta}{2}}\right)\Delta\lambda^2_{1/e} \tag{5}$$

where m_e is the resting electron mass, c is the speed of light in a vacuum, and $\lambda_{1/e}$ is the $1/e$ half-width of the Gaussian fit spectrum. The T_e can also be extracted by plotting the natural logarithm of the spectral intensity vs. the wavelength shift squared, if a linear response is observed, then it is proportional to the inverse of the line's slope through the following relationship [40,51,52].

$$Slope = \frac{-6.39\ x\ 10^4}{\lambda_i^2}\left(sin^2\left(\frac{\theta}{2}\right)T_e\right)^{-1} \tag{6}$$

Following the same assumptions (Maxwellian EEDF and incoherent scattering) as when extracting the T_e, the n_e in the probed volume can be determined by integrating the spectral response area and absolutely calibrating the response to the Rayleigh scattering intensity I_R at a known gas density n_R via the following equation [52],

$$n_e = \frac{\int I_T d\lambda}{I_R}\left(\frac{\sigma^R}{\sigma^T}\right)n_R\left(1+a^2\right) \tag{7}$$

where $\sigma^R/\sigma^T$is the ratio between Rayleigh and Thomson cross-sections.

Unfortunately, deviations of the EEDF from Maxwellian equilibrium are seen in low-temperature and low-pressure plasmas due to non-LTE conditions, and thus a Gaussian profile no longer accurately represents the relationship between the spectral response and the EEDF shape. A simple method to relate the Thomson scattered spectrum directly to the EEDF shape has been previously reported by Huang et al. [39] which involves plotting the change in intensity of neighboring spectral channels as a function of the observed wavelength shift squared.

2.2. Experimental requirements

TS measurements are difficult to perform based on the inherently small cross-section for Thomson radiation, the many orders-of-magnitude higher Rayleigh scattering signal intensity centered at the peak laser wavelength, the presence of large amounts of stray light, and the need to maintain the plasma integrity without perturbation when probing the species present. The Thomson scattered differential cross-section across a solid angle typically has values ranging between 10^{-29} and 10^{-31} m^2 sr^{-1} as seen by Eq. (3). In comparison, the Rayleigh scattered differential cross-section can be many orders-of-magnitude higher, commonly 10^7 times or greater in difference, shown by Eq. (2), which places a large burden on spectral contrast (ratio between the intensities at various wavelength shifts in relation to the central Rayleigh peak) close to the laser wavelength. Extremely close wavelength shifts are seen in many plasmas used for chemical analysis due to the majority of probed electrons being thermalized thus having relatively low T_e, commonly less than 1 eV [11,16,17,29,37]. It is imperative that the Rayleigh scattering signal is minimized to permit implementation of appropriate detector gain levels to realize Thomson measurements and prevent detector saturation. Stray light, often originating from the high-powered laser light reflecting/scattering off various surfaces, effectively increases noise across the entire resulting spectrum and can problematically lower the signal-to-noise ratio to unacceptable levels.

Based on the expanded upon criteria for TS measurements, a wavelength selection instrument must be utilized that has the ability to maximize optical throughput, have high spectral contrast at wavelength shifts close to the laser wavelength and minimize stray light levels simultaneously. Moreover, the plasma of interest must be considered when designing an experimental setup. Triple grating spectrographs (TGS) are well suited for measurements on low-density plasmas ($n_e \leq 10^{14}$ cm^{-3}) of which there have been a few designs reported to date [37,53]. For example, Finch et al. very recently described a TGS that features an f-number of F/2, spectral resolution of ~0.6 nm, contrast $\leq 10^{-6}$ at 532 ± 0.5 nm and stray light rejection (~1.8×10^{-8} at 22 nm − 32 nm above and below 532 nm), with the lowest limit-of-detection in terms of n_e reported to date of ~10^9 cm^{-3} when measuring chemical analysis plasmas at ~1 eV T_e [54]. On the other hand, single monochromator setups (many of which are commercially available) are more suited to higher-density plasma measurements ($n_e \geq 10^{14}$ cm^{-3}) and a couple have been described recently [42,55]. For example, Zhang et al. recently used a commercial spectrometer (Andor, Shamrock 500i) equipped with an iCCD camera (Andor, DH334T-E3) that has an f-number of F/6.5 and a spectral resolution <0.1 nm [56], while being able to detect n_e of ~3×10^{16} cm^{-3} at ~1 eV T_e [42]. Furthermore, in observation of the extremely small TS cross-sectional area, a relatively high laser intensity must be used to obtain a large enough photon flux for measurement purposes. Nevertheless, plasma perturbations due to heating effects involving interactions between high energy lasers and plasmas have been problematic for deterministic energy studies [44,57]. Multiple studies have been performed in which the primary intermediaries contributing to plasma heating are shown to be electron-ion collisions after inverse bremsstrahlung processes within thermal plasmas and electron-atom collisions in non-thermal plasmas [12,58–62]. The criteria to avoid plasma heating effects was revisited in a paper by Carbone et al. in 2012 that defines the relative increase in electron temperature, assuming the refractive index of the plasma is 1 and the square of the lasers' angular frequency ω_{laser}^2 is greater than the square of the collision frequency, for electrons with heavy particles ν_{eh}^2 by the following expression [63],

$$\frac{\Delta T_e}{T_e} = \frac{2E_1 \nu_{eh} \omega_{pl}^2}{3Ac\omega_{laser}^2}\left(\frac{1}{n_e k_B T_e}\right) \quad (8)$$

where E_1/A is the incident laser fluence and ω_{pl} is the angular electron plasma frequency. Preventing plasma heating is necessary as the fractional increase in the T_e is directly proportional to increasing the laser fluence, as seen by Eq. 8, and is the only controllable external parameter other than the laser wavelength, which is typically non-tunable. In addition, it has also been recently shown that when using high laser fluences (10^{16}–10^{17} W x m^{-2}) and a laser pulse duration >1 ns, the error in measuring the n_e can significantly increase (~10–20%) when analyzing plasmas with $T_e = 1$ eV and $n_e < 10^{10}$ cm^{-3} [57]. In a low-pressure plasma, the electron's mean-free path is often on the same order of magnitude as the laser beam radius used in TS studies (< 1 mm). This gives a displacement time of <1 ns for electrons near the laser beam to move out of the detection volume by ponderomotive forces [64]. Therefore, the increase in error at laser pulse widths >1 ns is due to the number of electrons in the detection volume effectively decreasing during the scattering measurement while displacement by ponderomotive forces occurs.

3. Insights gained through selected Thomson scattering studies

3.1. Inductively coupled plasmas

Inductively coupled plasmas (ICPs) are an effective analytical tool, specifically pertaining to elemental analysis [65]. ICP diagnostics performed via TS studies for spectrochemical analysis were pioneered by Hieftje and co-workers (Sesi et al. [66], Marshall et al. [67,68], Huang et al. [39,40,69]), furthered by van der Mullen and de Regt [70–72], and have been covered in previous reviews [11,15]. It is important to note that relatively high n_e (~10^{14}–10^{15} cm^{-3}) are typically encountered in ICPs implemented for elemental analysis, thus less stringent instrumentation such as single monochromators can be successfully used for TS diagnostics. A couple of selected TS studies that have not been previously reviewed will be briefly discussed to illustrate.

Coupling the ICP with mass spectrometry (MS) offers several advantages including simultaneous multi-elemental analysis (with appropriate mass analyzer e.g. time-of-flight), low limits of detection, a wide dynamic range, and the ability to perform isotopic analysis [65,73]. However, ICPMS is known to suffer from matrix effects that are not well understood in the upstream region of the MS interface. Gamez et al. implemented Thomson and Rayleigh scattering plasma diagnostics to assess the effect of exposing the tail of the ICP to a MS sampler, as a function of varying operating conditions, including ICP radiofrequency (RF) power and central-gas flow rate, as well as MS sampler pressure and sampling depth [74,75]. The fundamental electron characteristics were measured in the presence and absence of the MS sampling interface, which allowed for a more representative picture of the underlying changes seen during ICPMS analyses. The authors used a single monochromator setup, previously described by Sesi et al. in 1997 [66], where the spectral image was shifted to focus the laser wavelength just outside the iCCD detector's active area. This allowed half the Doppler broadened TS spectrum to be measured on one side, without the Rayleigh signal causing saturation.

Fig. 2 displays the effects of varying levels of RF power on n_e and T_e at various radial positions. It is apparent that n_e and T_e both increase with increments of applied RF power. These radial profiles display a low n_e and T_e at the axis, which subsequently increases with radial distance. Furthermore, the n_e is lower with the MS sampling interface than without it at 0.75 kW (Fig. 2A). However, the reverse trend is observed at 1.5 kW (Fig. 2B). It was postulated that the MS interface was

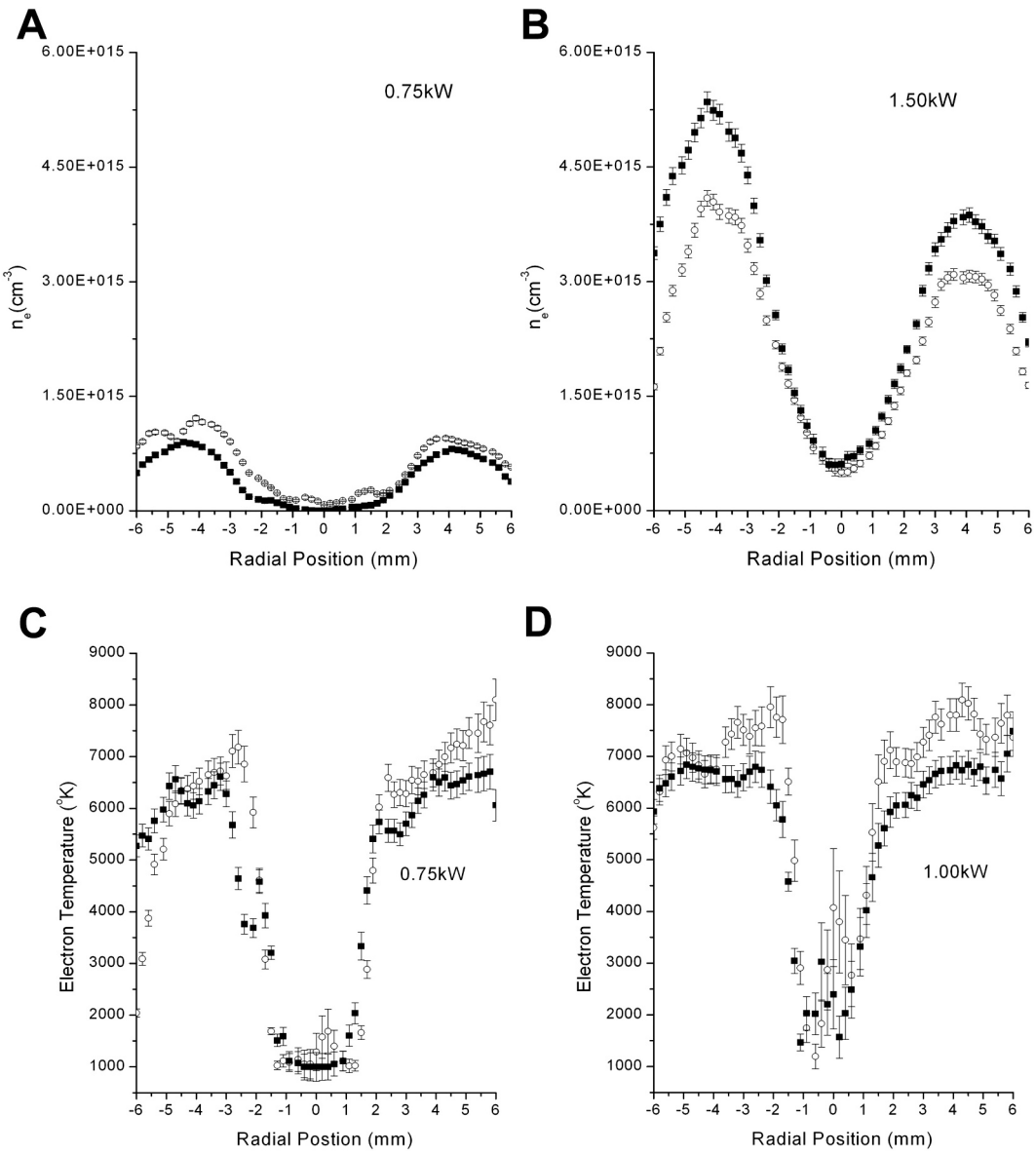

Fig. 2. Radial profiles displaying n_e values at (A) 0.75 kW and (B) 1.5 kW of RF power applied and T_e values at (C) 0.75 kW and (D) 1.00 kW of RF power applied during the introduction of a 0.1 mM Ca solution observed from 7 mm above the load coil (ALC) with (■) and without (○) the MS sampling interface [75]. Adapted by permission of Elsevier.

intercepting some of the applied power via eddy current creation, thus the effect is more noticeable at lower applied RF powers [75]. The overall T_e at 1.00 kW (Fig. 2D) is higher than that at 0.75 kW (Fig. 2C) which can be seen in both the central channel and the outer regions, though it is more drastic at the axial position. The introduction of the sampling interface generally causes a decrease in T_e, which can be seen in Fig. 2C-D. This effect can also be explained by the interception of applied power by the MS interface previously mentioned. Another hypothesis to explain the lower T_e is that the interface can behave as a heat sink [74].

Fig. 3A-B display the effects of varying sampling depths on the n_e as a function of radial position. The effects of central-gas flow rate were also measured, at the axial position and in the outer region of the plasma (4.9 mm), with and without the MS sampling interface (Fig. 3C). Overall, the n_e drops with an increase of central-gas flow rate, though it is much more pronounced around the axis of the plasma. The effects of sampling depth were then observed at 6 mm below the sampling cone. At a sampling depth of 13 mm above the load coil (ALC), with a corresponding observation height of 7 mm ALC (Fig. 3A), the n_e has higher maxima at the outer regions of the plasma while being lower in the axial position when compared with a sampling depth of 17 mm ALC (Fig. 3B) and a corresponding observation height of 11 mm ALC. Furthermore, the effects of the sampling interface on the electron distributions are more pronounced at a 17 mm ALC (11 mm ALC observation height) sampling depth.

Overall, changing the ICP operating conditions was shown to have varying effects on the plasma's electron parameters. Significant changes were also observed in the presence of the MS sampling interface. Generally, the T_e and n_e in the upstream region of the ICP were seen to increase with increasing RF power (Fig. 2A-D). The increased n_e in the outer regions of the plasma when the interface is present, together with lowered T_e and T_g, indicates that the rate of ambipolar diffusion was reduced, leading to a slower decay of the plasma. Additionally, the interface also produced an increasing disparity between the T_e and T_g with increments of applied RF power, which is an indication that the interface detracts the ICP further from LTE [75]. The authors also observed that increased RF power leads to increased lateral diffusion, as shown by changes in measured Ca^+ number densities, while addition of

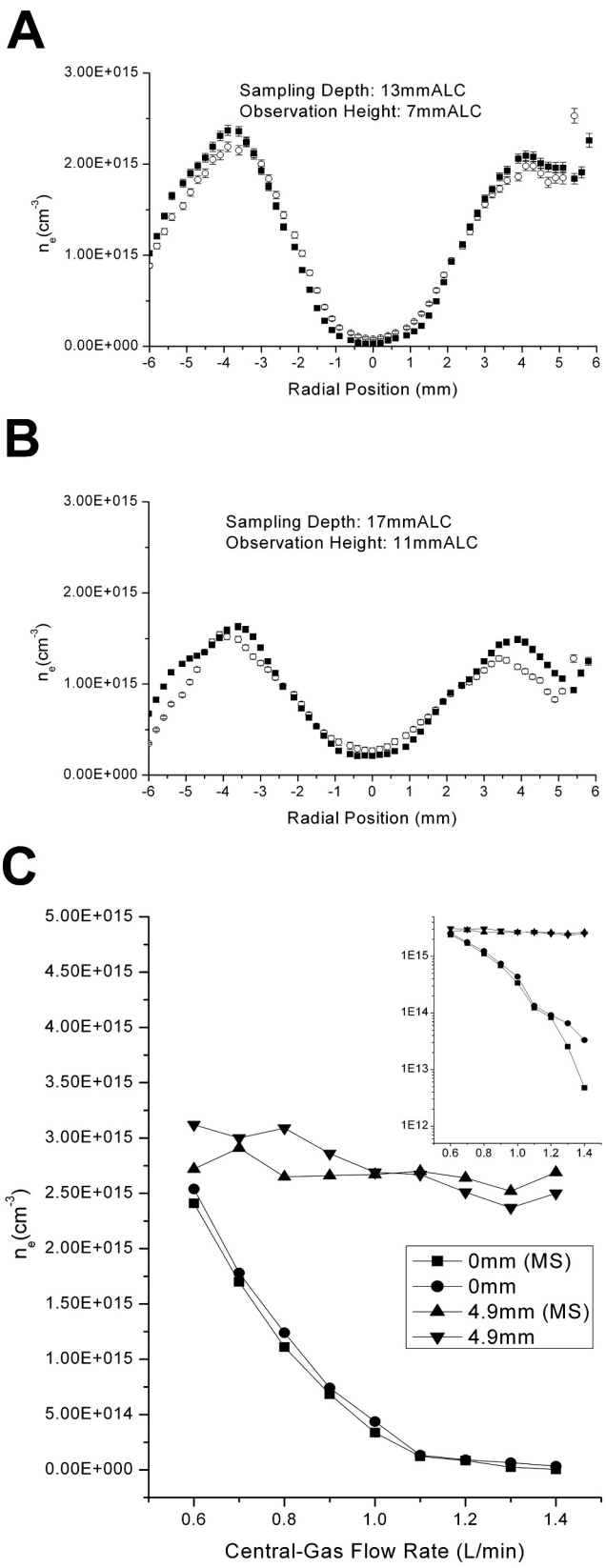

Fig. 3. Effects of varying sampling depths at (A) 13 mm ALC and (B) 17 mm ALC on the n_e with a central-gas flow rate of 1.1 L/min and observed from 6 mm below the sampling cone with (■) and without (○) the MS sampling interface. (C) Displays the effects of central-gas flow rate on the n_e from an observation height of 7 mm ALC in the outer regions of the plasma at 4.9 mm and in the axial position with and without the MS sampling interface [74]. Adapted by permission of Elsevier.

Li as a matrix further lowered the Ca^+ at the axial position, possibly due to earlier vaporization coupled with a shift in ionization equilibrium. In addition, evacuating the region behind the MS sampler was shown to increase n_e 1–2 mm upstream from the sampler tip towards the axial location [75].

A decrease in n_e was observed at higher central-gas flow rates (Fig. 3C). These effects are more prominent in the axial position of the plasma. Also, it was determined that at central-gas flow rates below 1.0 L/min, the presence of the MS interface would lower n_e values. T_g were also shown to be lowered in the presence of the MS interface [74]. The authors conclude that care should be taken when using MS-based diagnostic techniques to obtain insights into mechanisms of an ICP not perturbed by an MS sampler.

Other authors have also recognized the importance of understanding the effects of the MS interface on the upstream ICP. For example, Farnsworth and co-workers used laser-induced fluorescence to monitor metastable ion and ground state ion number densities and showed, among other insights, that their ratio is lowered in the presence of the MS interface, which indicates lower excitation temperature (T_{exc}). [76]. Aghaei et al. studied the effects of an MS sampling cone via computational methods and observed increasing n_e values in the central region of the plasma with increments in the distance of the sampler cone from the load coil [77], in agreement with experimental studies performed by Gamez et al. [74].

3.2. Glow discharges

Glow discharges (GDs) have been widely used for the direct elemental analysis of solids, throughout a wide variety of applications [5,78]. These plasmas offer many advantages, including high-throughput (fast sputtering rates) simultaneous multi-elemental analysis, low operating costs, depth-profiling capabilities, and the ability to perform accurate analysis on low mass elements while the majority of other techniques fall short [2,4,6,8,79–82]. Several plasma diagnostic studies have been performed on GDs under conditions relevant for chemical analysis, in an effort to better understand the underlying mechanisms [27,83]. Some of those studies include measurements of T_g and n_e via Doppler and Stark broadening [84], respectively. Other studies measured T_e, n_e, and EEDF via Langmuir-probes [27,31,32,85].

There are also some studies that report T_{exc} which gives an indication of the energy distribution pathways [27,86–88]. However, it should be noted that typical GD operating conditions for OES and MS analysis include low pressures, which leads to further deviations from LTE and a lower n_e, as a consequence of the reduced number of collisions [89]. On one hand, the more pronounced deviations from LTE mean that T_{exc} and ionization temperatures (T_{ion}) are not very reliable for deducing T_e. On the other hand, the lower n_e in GD requires instrumentation with better contrast, stray light rejection and light throughput to achieve accurate TS measurements.

In 2003, Gamez et al. first reported an instrument to perform laser-scattering fundamental studies on GD under typical conditions used during chemical analysis (Fig. 4A) [36]; the T_e, n_e and EEDF were obtained via TS and T_g was obtained via Rayleigh scattering [36]. A Nd:YAG laser (probe beam) at 532 nm was directed to a GD chamber equipped with several features for restricting stray light, such as entrance and exit windows set at Brewster angle placed far from the observation region, a series of baffles inside the extended arms, a pair of irises to cut the divergent light around the beam, and black paint lining the inside of the GD chamber to reduce the reflectivity of the walls. All these practices resulted in a low stray light level of ~350 mTorr of Ar gas. This is an excellent example of the stray-light minimization when compared to a previous ICP plasma diagnostic system used by Sesi et al. which achieved a level of ~11 Torr [66]. The double monochromator (SPEX 1403, f/6.9) used was also able to provide a high contrast of $\sim 10^{-6}$ at 1.4 nm wavelength shifts. The sensitive, PMT-based, gated

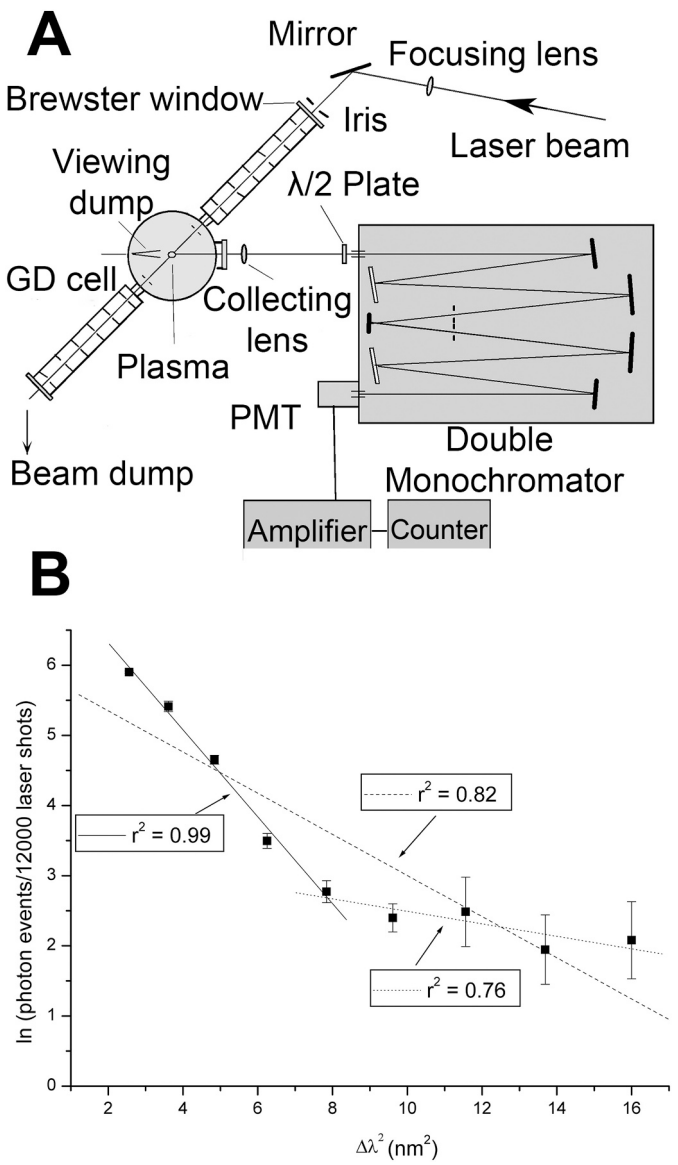

Fig. 4. (A) Schematic of the laser-scattering instrument for characterizing GDs. (B) Linearized TS spectrum showing 2 distinct groups of electrons (thermalized and high-energy) [36]. Adapted with permission from The Royal Society of Chemistry.

photon-counting system allowed weak signal detection, while lowering the overlapping plasma background radiation measured. The planar-cathode GD geometry consisted of a 1.2 cm diameter Cu cathode and a 5.0 cm diameter stainless steel anode, with an interelectrode distance of 5 cm.

As aforementioned, GD is not in LTE, which results in different species having different temperatures. Fig. 4B shows that when a TS spectra from the GD is plotted as ln(scattered signal) vs $\Delta\lambda^2$, it does not yield a single linear relationship which, as explained previously (Section 2.1), would be the case when a single Maxwellian distribution describes the EEDF. Instead, the wavelength shifts closer to the laser line fit one line, corresponding to a low-energy electron group, and the further wavelength shifts fit a second line, corresponding to a high-energy group. The T_e (0.42 ± 0.03 eV, $r^2 = 0.99$) from the low-energy electron group was observed to be comparable to other studies using different techniques [27,90]. On the other hand, the corresponding n_e ($1.75 \pm 0.21 \times 10^{13}$ cm^{-3}) was different from the literature values and this was assigned to disparities between operating conditions (Grimm type vs planar-cathode) or drawbacks from the particular diagnostic technique utilized (e.g. Langmuir probe perturbations) [27]. The capability to obtain EEDFs from the TS spectra was also shown, determined by the method developed by Huang et al. [39] described in section 2.

Gamez et al. used the instrument described above to perform a systematic fundamental study on a direct current (DC) GD [28]. The study focused on the axial profiles (4 mm to 23 mm from the cathode) of T_g, T_e, n_e and EEDF obtained under a variety of operating conditions (pressure: 1 Torr vs 3 Torr, voltage: 515 V vs 880 V, and current: 2.5 mA vs 10 mA). Another parallel study by Bogaerts et al. compares these experimental results to those obtained with theoretical computational models [26], including Monte Carlo methods, fluid dynamics, heat conduction models, and others, selected due to their direct relevance for the Ar gas and electron characteristics. In this section, more efforts will be focused on the experimental part of the study.

It is reported that at any given set of operating conditions, T_g decreases, in the range of 1000 K to 273 K, as the probing distance from the cathode surface increases. Also, at any given pressure, T_g is directly proportional to the applied current and voltage. When the current is kept constant at 10 mA, the T_g is lower at the higher pressure (3 Torr) compared with 1 Torr. Meanwhile, the voltage is reported to be lower at 3 Torr, indicating less resistance in the plasma through Ohm's law, which was considered as the reason for the decreased T_g. Similar trends that these parameters have on T_g are also reported in other studies [30,84,89,91,92], despite the differences in operating conditions. It is noteworthy to mention that the authors could not measure T_g closer than 4 mm to the cathode due to the high levels of stray light generated.

The experimental results also agree with theoretical values based on computer modeling developed by Bogaerts et al. [26]. The calculated T_g is nearly linear with the assumed cathode temperature, which may be a weakness of the model since it is very difficult to directly measure the actual temperature of the cathode. Thus, the cathode temperature is corrected with the T_g distribution, which results in a better fit of current-voltage-pressure. Overall, the study shows that the experimental data and the computational data are in reasonable agreement after taking into account operational differences.

T_e results show that at a particular set of operating conditions, greater deviations from a single-Maxwellian behavior are observed closer to the cathode surface. At closer distances (4 mm, 6 mm and 8 mm), it is obvious that two distinct groups (high-energy electrons and low-energy electrons) are present. The measured EEDF results (Fig. 5A) show the distribution of low-electron energies is relatively constant at increasing cathode distances, while the population of high-energy electrons drops below the n_e detection limit. When the current and power are reduced (from 55 mA to 35 mA, 1 kV to 520 V), fewer low-energy electrons are observed at further distances, which the authors suggest may be due to the increased collisional frequency between Ar and electrons, given the higher Ar number density related to the lower T_g measured. Modeling results by Bogaerts et al. [26] shows that the comparison between the experimental data and the calculated data cannot be directly made. This is because the model calculated EEDF is more suitable for high-energy rather than low-energy electron groups, and as mentioned before, experimental TS was unable to record the high-energy electron groups due to the n_e detection limit.

The measured n_e of the thermalized (low-energy) electrons (Fig. 5B) decreases as the distance to cathode increases, while high-energy electrons can only be observed when the distance to the cathode is <8 mm. The n_e from both the computational model and TS, at 3 Torr, 55 mA, and 1000 V, present much smaller values when near the cathode [26]. A maximum n_e was observed in the computational model where the negative glow begins (1 mm from the cathode) and deceases significantly until 20 mm from the cathode, giving a 'peak' shape. However, under 3 Torr, 55 mA, and 1000 V conditions, the experimental results do not show this 'peak' shape, which can be contributed to the inability to measure closer than 4 mm to the cathode surface as mentioned previously.

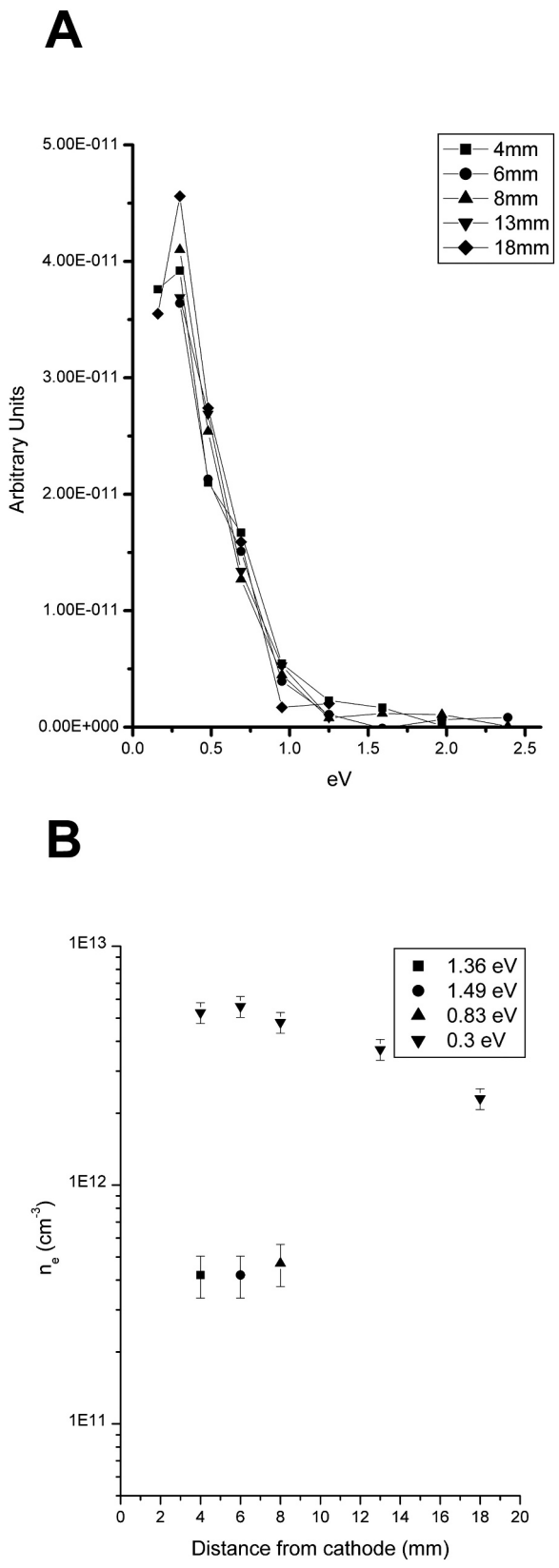

Fig. 5. (A) The EEDF at various axial positions, where regardless of cathode distance, the low-energy electrons have a higher population than the high-energy electrons. (B) The n_e at different distances from cathode, also showing that the population of the lowest energy electron group is higher than the higher energy electron groups. Results shown were obtained with the GD at 3 Torr, 55 mA and 1 kV [28]. Adapted with permission from Elsevier.

In 2006, Gamez et al. conducted a systematic investigation on the fundamental parameters (T_g, n_e, EEDF, and T_e) for ms-pulsed DC GDs, taking advantage of the inherent spatiotemporal resolution of TS [29]. Pulsed GD has been found to lower cathode heating effects, which allows the application of higher instantaneous powers, resulting in strengthening the excitation and emission processes [93]. Different pulse time-regimes can offer unique advantages [94], such as measuring lower background during the afterglow or accessing different ionization pathways in the prepeak (electron impact) and afterglow (Penning ionization) to yield elemental, structural and molecular information. Nevertheless, the underlying mechanisms under pulsed GD conditions are not completely understood. In this work, the aforementioned TS instrument design [36] was upgraded with an iCCD, instead of a PMT, for simultaneous signal detection from multiple spatial positions. Measurements were performed using a 5 ms GD pulse duration at 1 Torr (13 mA plateau, 820 V plateau) and 3 Torr (75 mA plateau, 920 V plateau). The T_g observed during the prepeak was related back to the temporal profiles of the current, while T_g measurements during the plateau agreed with the two previous DC GD studies using the same instrumentation after normalizing the current and voltage [26,28].

The T_e and n_e from the observed higher energy electrons, are shown in Fig. 6. It is evident that T_e in the prepeak (0.2 ms) is lower than at the plateau (4.9 ms), while the opposite trend was reported for the T_e of the low-energy electron group. The n_e of the high-energy electron group (Fig. 6B) is higher at the prepeak than the plateau, while the opposite trend was also reported for the n_e of the low-energy electron group. The authors attributed these trends to the voltage effects on T_e. For example, when the pulse starts (prepeak), the voltage will slowly rise and the relatively lower T_e of the high-energy electron group (found earlier in the pulse before the plateau) will result in more favorable collision cross-sections, thus improving energy transfer and resulting in higher T_e for the thermalized electron group.

During the pulse plateau, it was shown that n_e decreases at farther distances from the cathode. On the contrary, in the afterglow region (5.2 ms), the n_e value increases from 4 to 6 mm from the cathode. In addition, the ratio of n_e in the afterglow to the plateau (4.9 ms) is lower, closer to the cathode. The authors propose that this is due to the increase in the Ar metastable number density at certain positions in the afterglow, leading to a higher degree of Penning ionization. Furthermore, the low n_e measured in the afterglow puts in question the significance of the collisional-radiative recombination mechanism ($Ar^+ + e^- + e^- \rightarrow Ar^* + e^-$) for the formation of Ar metastables, because the reaction rates associated with that pathway require a considerable increase in n_e. Thus, the authors propose that dissociative recombination of Ar dimer ions ($Ar_2^+ + e^- \rightarrow Ar^* + Ar$) will play a more significant role than previously considered [95]. Moreover, a follow-up study conducted by Bogaerts [96] considering which mechanisms contributes the most for the formation of Ar metastables in the afterglow in pulsed GD, further supported the significance of dissociative recombination of Ar dimer ions.

3.3. *Laser induced plasmas*

Laser induced plasmas (LIPs), especially those used for laser-induced breakdown spectroscopy (LIBS) have become very popular in recent years due to their inclusiveness to a wide variety of samples types (organic and inorganic) that can be analyzed, little-to-no sample preparation, stand-off/remote sensing and elemental mapping capabilities [25,97–101]. However, the quantitative nature of LIPs (especially calibration-free techniques) can only be accurately realized if an extensive knowledge of the fundamental species densities and temperatures is available. The need for this underlying knowledge comes from the highly complex laser-sample-plasma interactions that are known to have drastic spatiotemporal changes. Nevertheless, there are significant discrepancies seen between different theoretical modeling approaches and experimental observations of LIPs, thus providing a need for more accurate and reproducible plasma diagnostics techniques [42,55,102].

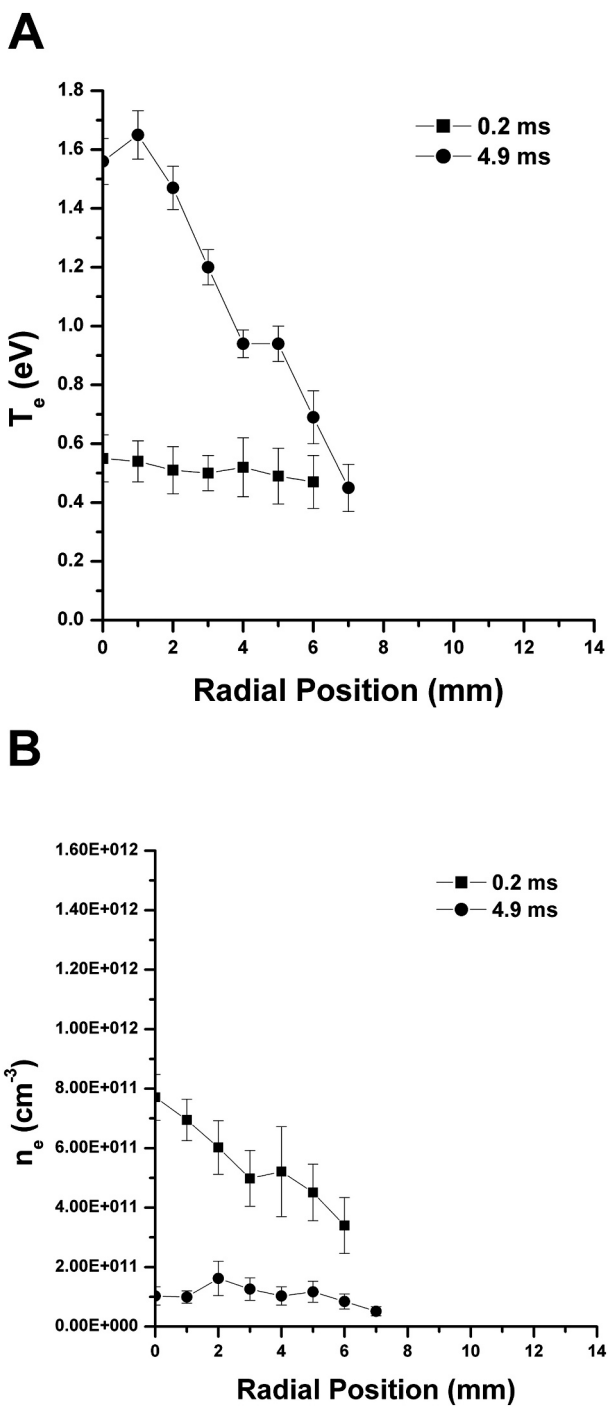

Fig. 6. (A) Shows the relationship between the high T_e group at different pulse times vs. the radial position. (B) Shows the relationship between the high-energy groups' n_e at different pulse times vs. the radial position. Results shown were obtained with the GD at 1 Torr, 13 mA and 920 V with the error bars representing one standard deviation [29]. Adapted with permission from The Royal Society of Chemistry.

TS has already provided many insights into the fundamental species parameters and underlying mechanisms as a function of space and time for LIPs, which have been highlighted in a 2014 review published by Dzierżęga et al. [25]. It is noteworthy to mention that relatively high n_e values are found in LIPs and thus the instrumental requirements are less stringent than when analyzing plasmas with much lower degrees of ionization. Studies have been successfully performed using only single monochromators as wavelength selection instruments, rather than double or triple spectrometers [42,55]. Some selected TS studies on LIPs that have taken place since the 2014 review will be presented here to show the newly gained insights.

In 2015, Nedanovska et al. performed a spatiotemporally resolved study of the expansion dynamics of a LIP operated in atmospheric He [103]. Plasma creation was performed in 1 atm of He using 9 ns, 140 mJ laser pulses focused to 10^{11} W × cm^{-2}, from a 1064 nm Nd:YAG laser operating at a 10 Hz repetition frequency. Scattering measurements were performed using a second Nd:YAG laser to probe the LIP orthogonally (parallel to entrance slit of double spectrometer for radial information) at 532 nm using 7 ns, 80 mJ pulses focused to ~400 μm at 10 Hz, while the scattered light was collected via a double spectrometer. Thomson and Rayleigh scattering images were collected for time delays of 400 ns to 22.5 μs after the breakdown occurs and absolute calibration was performed using Rayleigh scattering on Ar as described by Sneep et al. [45]. The overall plasma behaviors observed were similar to previous studies performed in N_2 and Ar, with the exception of the toroidal structure forming at a significantly shorter time from the breakdown when sustained in He [104,105]. The authors note that this torus is formed between ~7.5 to 10 μs after the breakdown occurs and is due to the much smaller mass of He in relation to the other two gases previously studied for LIPs. In the center of the LIP starting at 2 μs the values for n_e are found to monotonically decay from 3.3 × 10^{23} m^{-3} to ~1 × 10^{20} m^{-3}, with a change in T_e of nearly 3 eV over the first 15 μs with two distinct trends; first a rapid decay from 400 ns to 1 μs and then a slower transient decay until about 7.5 μs when a second rapid decay is seen until 15 μs. The second rapid decay corresponds to the time when the toroidal structure is seen to form and an influx of cool gas molecules can quickly quench the n_e and T_e values. These results are in good agreement with simulations performed by Ghosh et al. that show the flow will reverse direction along the LIP axis, bring cooler molecules from the ambient air into the central portion of the LIP, and create complex vortexes that result in the toroidal shape observed [106]. The torus expansion rate can be modeled by $R \sim t^{0.4}$ which is consistent with the behavior of a non-radiative spherical blast wave [107].

In 2019, Zhang et al. studied the late evolution characteristics of a LIP after the breakdown in air, especially the formation of a complex toroidal structure [42]. To create the plasma, a pulsed Nd:YAG laser operating at its fundamental wavelength (1064 nm) was focused to breakdown the ambient air using a 7 ns pulse width at 200 mJ. A second frequency-doubled pulsed Nd:YAG laser operating at 532 nm was used to probe the LIP via 6 ns, 50 mJ pulses focused to ~500 μm in an orthogonal orientation to the breakdown laser (c.f. Fig. 7A). The laser fluence of approximately 20 J/cm^2 was chosen to minimize the plasma perturbation effects that are seen through the process of electron heating as discussed previously (c.f. Eq. 8). The scattered radiation was collected perpendicular in relation to the breakdown and probe beams using a pair of achromatic lenses. The image was rotated 90° for alignment of the horizontal probe laser with the vertical entrance slit (allowing multiple radial positions to be probed simultaneously) of a commercial spectrograph that was equipped with an iCCD (Fig. 7A).

The Rayleigh signal was not attenuated but allowed to pass through the spectrograph and saturate the central part of the detector. It is important to note that the inherently high n_e and collective scattering nature (described previously) of LIPs make possible implementing an experimental setup with high stray light and low contrast around the central wavelength for TS measurements. TS images (normalized to the maximum signal) were obtained as a function of time from 1 μs to 20 μs after the breakdown of the air and are shown in Fig. 7B. There are very high T_e (~4.4 eV) near the axial position of the LIP at 1 μs delay, seen by the symmetric crescents, observed from the collectively scattered radiation, at approximately 7 nm wavelength shifts. These temperatures rapidly decay to ~2.4 eV at 2 μs delay and then more slowly decay to ~1 eV for the next 16 μs. The n_e follows a similar trend as a function of delay time with some notable differences. First, the n_e maximum (~2.75 × 10^{23} m^{-3}) is found at the axial position, 2 μs after the LIP breakdown and

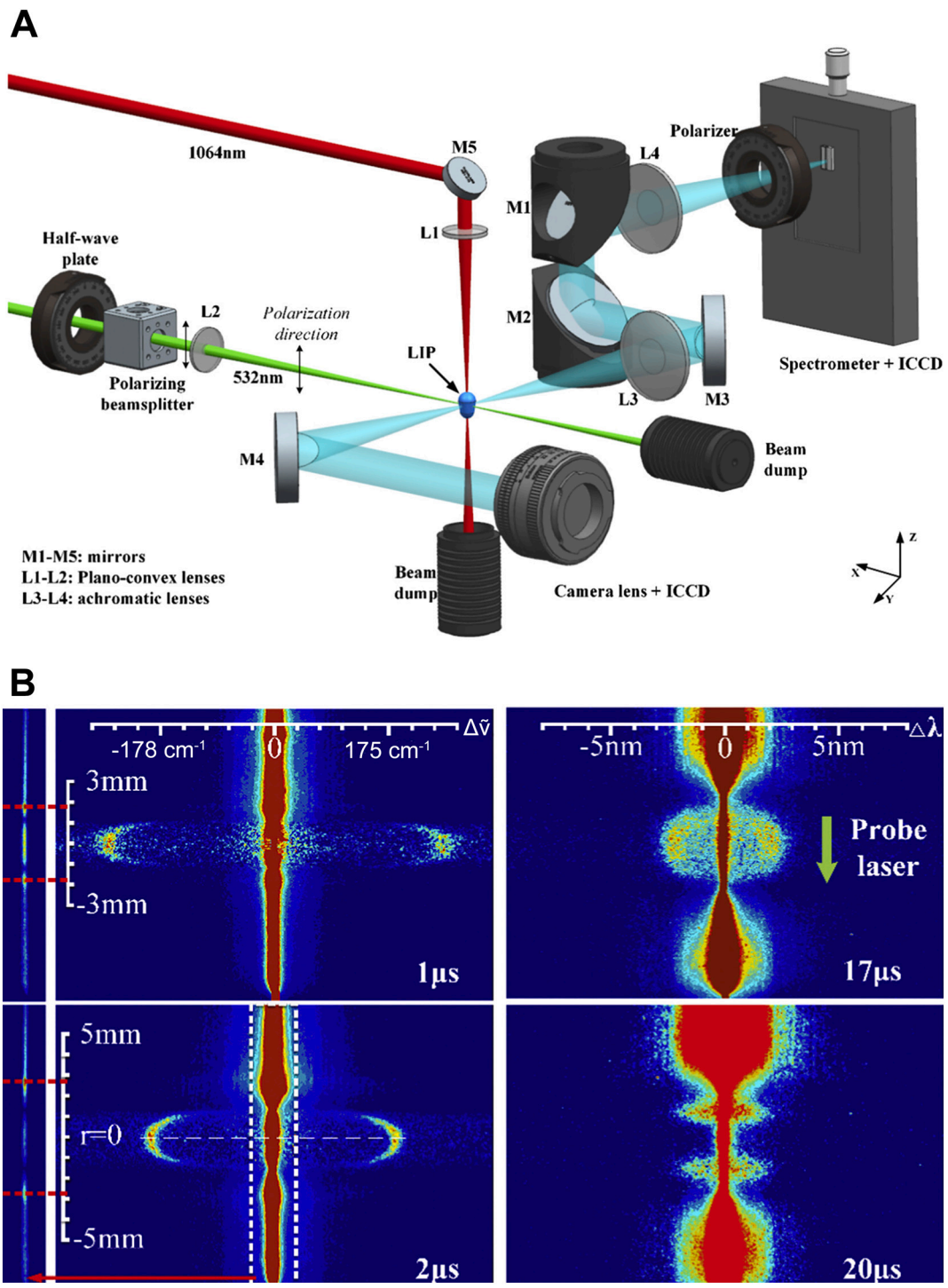

Fig. 7. (A) Experimental layout for TS measurements and self-emission studies on a LIP in air. (B) TS images taken at the center of the LIP at different time delays after the breakdown occurs. Spectral information is contained on the x-axis and spatial information along the probe laser beam on the y-axis. The saturated Rayleigh signal is seen by the strong line found in the center of the image and by lowering the gain can be clearly seen at the far left (B) [42]. Note the spectral scale is given in both frequency and wavelength for (B). Adapted with permission from Elsevier.

decreases by more than half in the next 3 μs. Furthermore, the n_e significantly changes as a function of radial position (seen by the lower intensities further from the axial position) whereas the T_e stays relatively constant radially for the first 17 μs. At 20 μs some interesting trends are seen in the scattering signal; two distinct peaks form off-axis symmetrically in the radial direction contributing to the almost complete formation of a complex toroidal structure (Fig. 7B). The T_e and n_e both reach their minimum at the axial position and their local maximum move radially outward to about ±2 mm. These results are in good agreement with those by Ghosh et al. described previously [106]. The trends in n_e and T_e are well modeled by decay curves using power laws up until 17 μs after the LIP breakdown, which corresponds to the initial formation of the toroidal structure.

In 2019, Dzierżęga et al. performed a comparative study using TS and two different Stark broadening models via the 696.5 nm Ar atomic line,

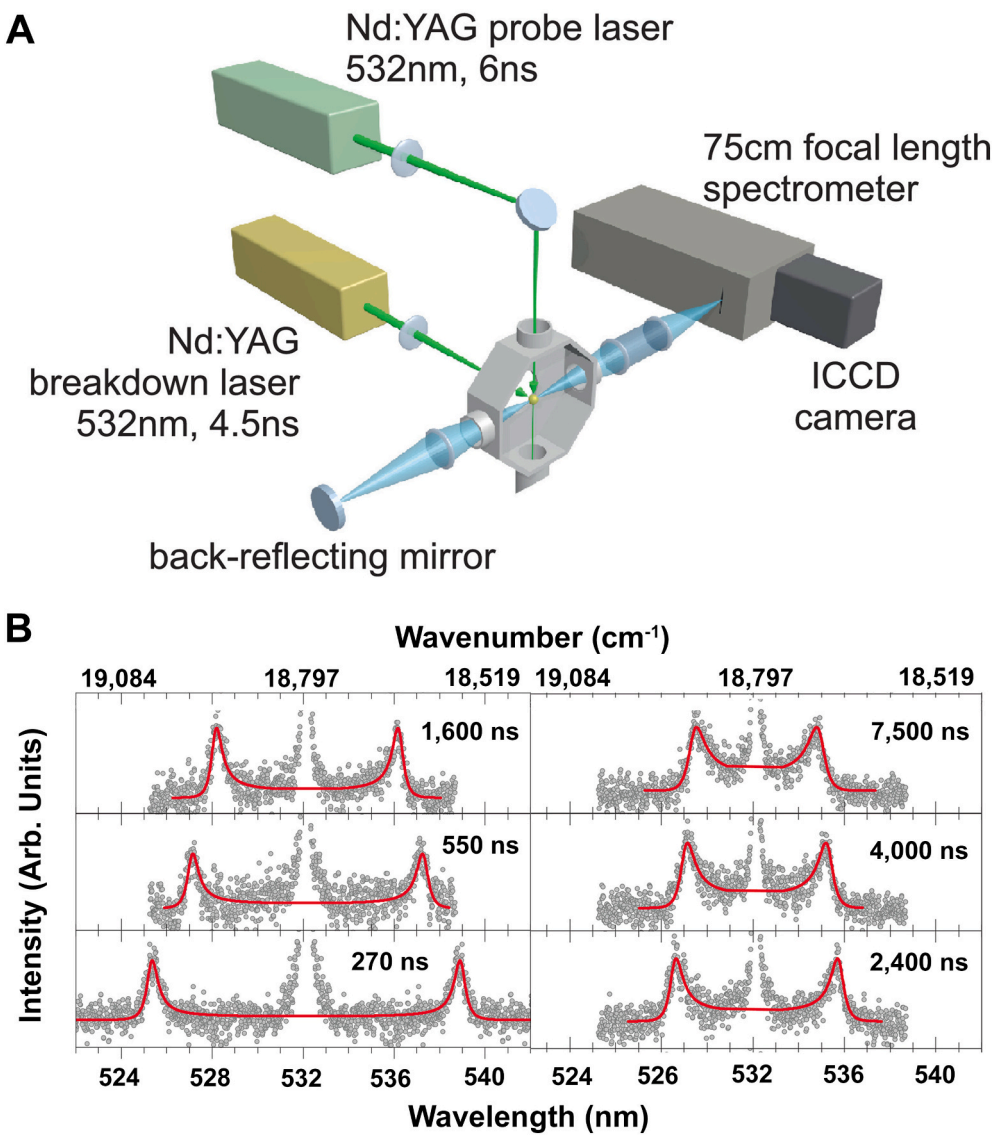

Fig. 8. (A) Experimental layout for TS measurements and self-absorption studies via the back-reflecting mirror method on a LIP in air. (B) TS spectra taken at different time delays, from 270 ns (bottom left) to 7.5 μs (top right) after the breakdown occurs. The Rayleigh peak is seen centered at 532 nm with coherent TS satellite peaks seen symmetrically shifted in in the wavelength dimension from center. The red line shows the fit with the spectral density function [55]. Adapted with permission from Elsevier. (For interpretation of the references to colour in this figure legend, the reader is referred to the web version of this article.)

for a LIP in a purely Ar environment [55]. The experimental setup used was similar to that by Zhang et al. that was previously described with the major difference being the reverse orientation of probe to breakdown laser geometry, thus eliminating the need for image rotation (Figs. 7A and 8A). A LIP was created by focusing a pulsed Nd:YAG laser operating at its second harmonic (532 nm) in the center of a vacuum chamber purged at 400 mbar with Ar. The breakdown laser utilized 4.5 ns, 15 mJ pulses at a repetition rate of 10 Hz focused to a beam diameter of 44 μm (Fig. 8A). A second Nd:YAG laser operating at 532 nm was employed to orthogonally probe the LIP plume using 6 ns, 10 mJ pulses focused to a beam diameter of 200 μm giving a fluence of 15 J/cm^2 (Fig. 8A). The scattered radiation was collected by a pair of lenses and focused onto the entrance slit of a commercial spectrograph equipped with an iCCD without the need for image rotation due to the probe laser's vertical orientation. A back-reflecting mirror was also implemented for performing self-absorption studies via the method described by Cvejić et al. in 2013 [108]. Fig. 8B shows the TS spectra (satellite peaks) at the central axial and radial position of the LIP as a function of delay time after the breakdown occurred. The central portion at 532 nm shows the Rayleigh signal that was not minimized and was allowed to pass through the spectrograph to the detector, once again showing the less stringent instrumental requirements for TS diagnostics implemented on LIPs. The n_e was observed to have a maxima of 3.67×10^{23} m^{-3} at 270 ns after the LIP breakdown and then decreases relatively consistently to 4.67×10^{22} m^{-3} over the next 7.23 μs. T_e values drastically decrease from ~4.95 eV at a 270 ns delay to ~2.39 eV just 280 ns later before slowly decaying to ~1 eV over the next 6.95 μs. Large discrepancies were found upon comparing the TS results to a computer simulated model performed based on the method by Gigosos and Cardeñoso [109]. These discrepancies are shown to increase as the n_e decreases and the authors propose this is most likely the cause of van der Waals broadening being neglected in their calculation, which contributes much more to the total line width than the Stark broadening due to the rapid rise in atomic species densities.

3.4. Microwave induced plasmas

Microwave induced plasmas (MIPs) have become attractive for use as ionization/emission sources in chemical analysis due to the wide diversity of geometries (surfatrons, Beenakker cavities, torches), cost-effective operation (especially when N_2 is used as the support gas), and the ability to tune the power based on the type/modality implemented [10,41,53,110]. The wide diversity of MIPs and the potential applications spanning many fields of interest leaves a desire for TS fundamental studies to be performed. Recently, TS was applied to two MIPs; one that is a surfatron operating in the ambient air and the second

designed as a torch sustained in N_2 [41,53].

In 2012, van Gessel et al. investigated a microwave surfatron launcher created in a ceramic tube, operating at an applied power of 50 W and a frequency of 2.45 GHz [41]. The end of the tube was exposed to ambient air and Ar was used to create a laminar flow inside. A previously constructed reflection-type TGS was used to optically filter the much stronger Rayleigh signal from the Thomson/Raman scattering and was described in 2002 by M. J. van de Sande and J. J. A. M. van der Mullen [37]. Further information about the TGS design considerations can be found in M. J. van de Sande's Ph.D. thesis [17]. Fig. 9A shows the schematic of the TGS which briefly consists of a notch filter created by two stages being set in subtractive mode with a physical mask placed in between, the image is rotated 90° prior to being imaged onto the vertical entrance slit for alignment with the laser axis, and finally the resulting spectrum is recorded by an iCCD. Due to the MIP being operated in ambient air, there are overlapping contributions of Raman from N_2 and O_2 and TS (c.f. Fig. 9B). The Raman spectra can be differentiated by calculating the total theoretical spectrum as a function of both contributing species. The fitting was performed in Matlab® and required knowledge of the partial air pressures and mixing ratios which was deduced by absolute calibration using Raman scattering on the ambient air without plasma. Fig. 9B shows the overlapping scattering contributions measured simultaneously at an axial position of 4.75 mm from the end of the plasma jet tube and the differentiation based on the previously described fitting procedure. Fig. 9C shows a 2D profile of the T_e that clearly shows a trend of increasing temperatures towards the "edges" of the plasma jet which can be explained by the laminar flow of cooling Ar in the center and the higher partial pressures of the ambient species at the "edges". Fig. 9D implies there is a maximum n_e at 2 mm axially from the tube's end, but the authors propose this is more likely an artifact that can be explained by the instability of the plasma jet seen visually near the tube's end. The 2D n_e profiles show an opposite trend to that of the T_e by decreasing towards the "edges" of the plasma jet. This could be explained by a higher degree of recombination when mixing with the ambient air and a lower degree of ionization. It is also noteworthy to mention that the 2D profiles of both T_e (Fig. 9C) and n_e (Fig. 9D) are shown to have increasing error with increasing radial position.

In 2017, Chalyavi et al. performed fundamental Thomson analyses on the plasma torch used in the Agilent 4200 MP-AES through the use of a custom high-throughput TGS, built in the Agilent laboratory [53]. The conditions used for the electron parameter analysis were 1 kW of applied

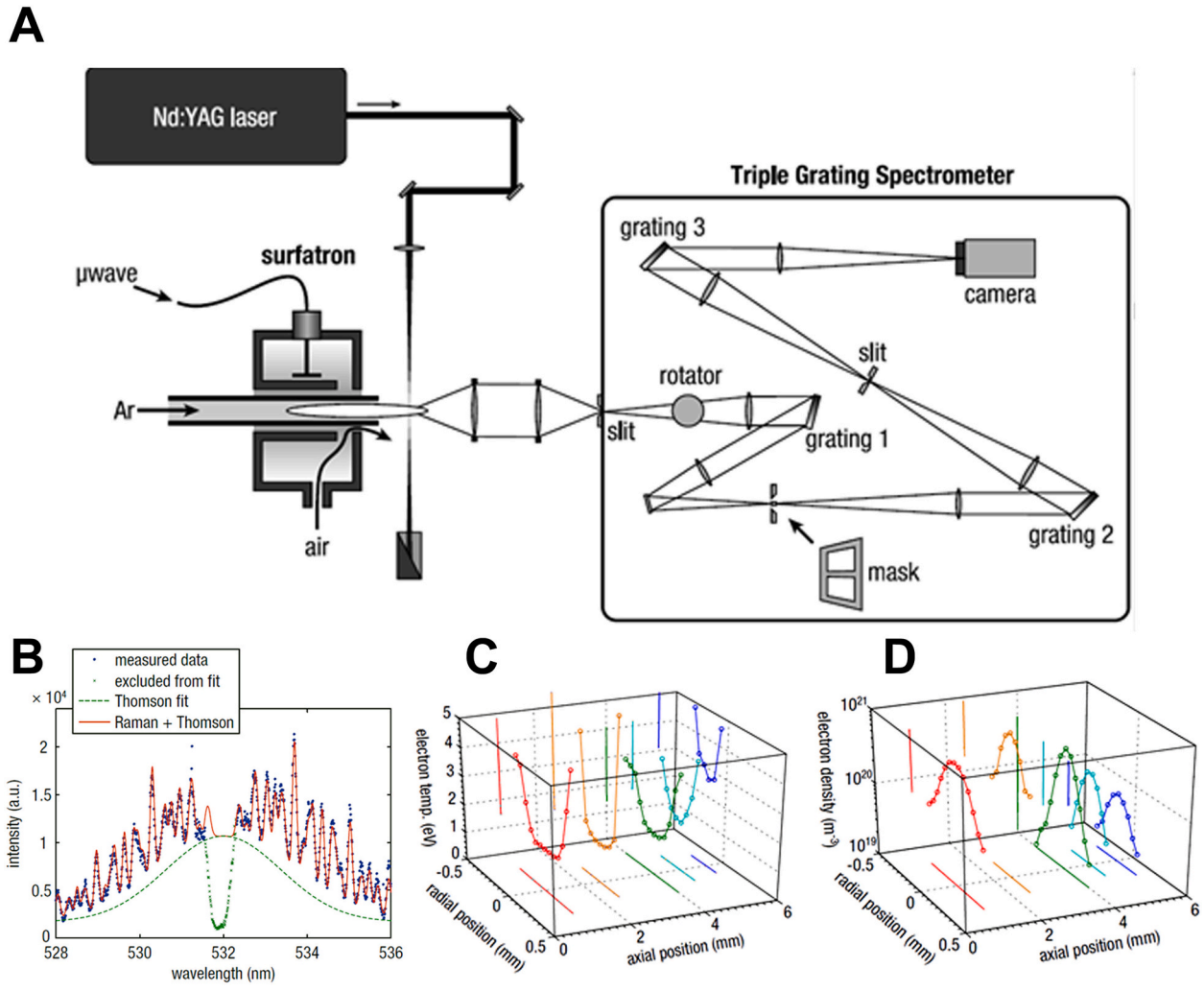

Fig. 9. (A) Experimental layout showing the microwave surfatron launcher and the scattered radiation collected at 90° via a reflection-type TGS. The surfatron jet is drawn horizontally, but is actually vertically oriented. (B) Spectrum showing overlapping contributions from Raman and TS taken at the plasma axis, 4.75 mm from the tube's. The red line shows the fit to both the Raman and the Thomson signal, while the green dashed line shows the extracted Gaussian fit profile that is used to calculate T_e and n_e. 2D profiles of the T_e (C) and n_e (D). The 0 mm axial position corresponds to the tube's end and 0 mm radial position is the center of the plasma jet [41]. Adapted with permission from The Institute of Physics. (For interpretation of the references to colour in this figure legend, the reader is referred to the web version of this article.)

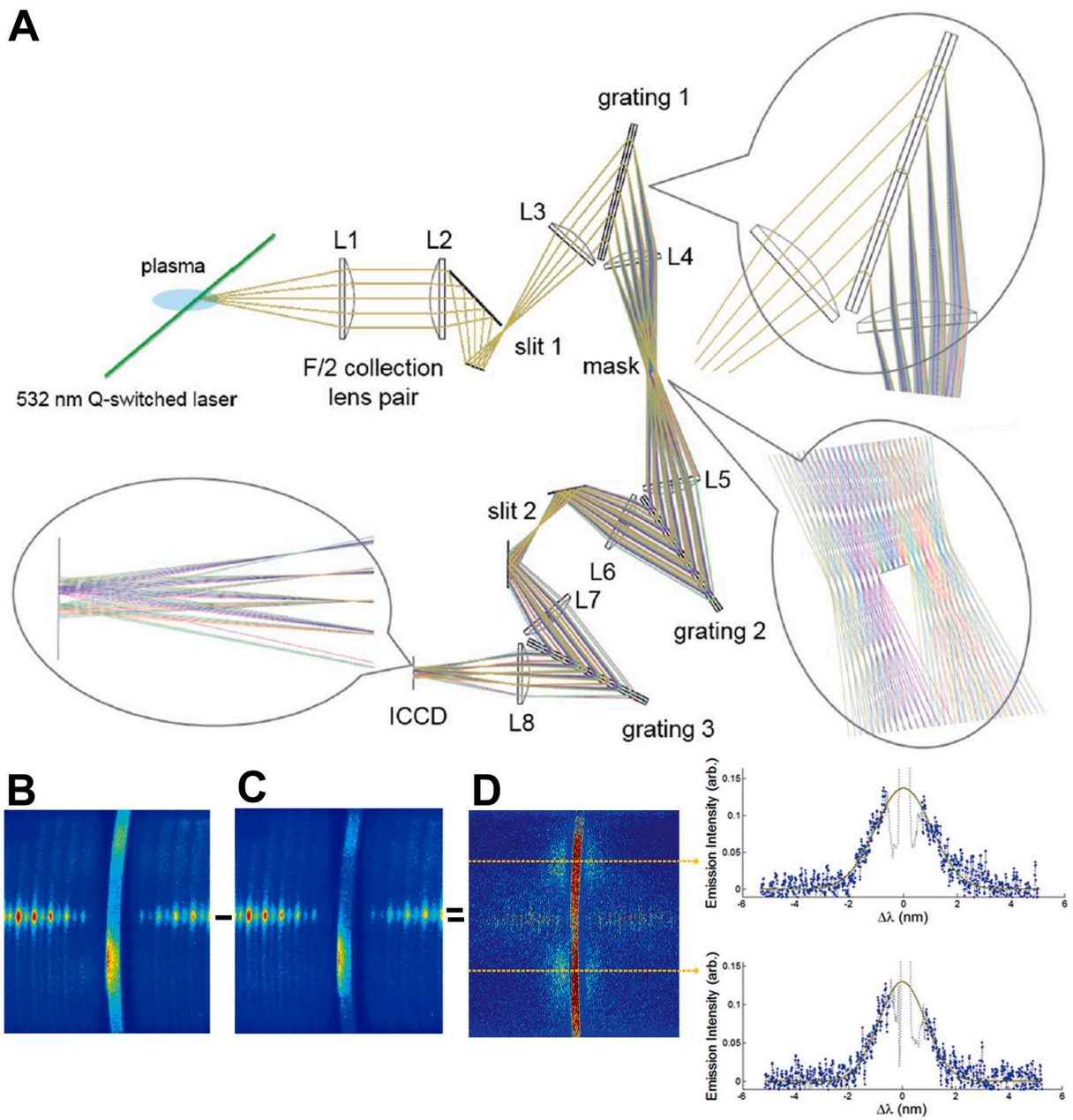

Fig. 10. (A) Optical layout of a custom−built transmission-type triple grating spectrometer. (B) Image collected at the iCCD (slit height vs. wavelength) with the remaining Rayleigh signal in the center and the outer fringes containing overlapping contributions from Raman and TS. (C) Image containing only the Raman signal in the outer fringes after removal of the TS by polarization control. (D) Raman-subtracted Thomson image with two profiles taken at different radial positions and 10 mm downstream from the sample inlet orifice. The blue dots show the experimental values included in the Gaussian fits and the dotted grey profiles are excluded from the fit due to the notch filter [53]. Adapted with permission from The Royal Society of Chemistry. (For interpretation of the references to colour in this figure legend, the reader is referred to the web version of this article.)

microwave power on a dry N_2 plasma that was probed using a Nd:YAG laser operating at 532 nm with 150–250 mJ, 7 ns pulses focused to 175 μm, at a repetition frequency of 30 Hz. The TGS (Fig. 10A) features a low f-number (F/2) collection efficiency with a transmission greater than 70% at 532 nm that is s-polarized. The first two stages are set in subtractive mode with a physical mask placed in between that minimizes the transmission for 532 ± 0.5 nm, effectively creating an efficient notch filter. The notch filter has an extinction efficiency on the order of 10^{-6} in the region mentioned previously, thus allowing close wavelength shifts to be measured from the incoherent Thomson signal. The scattered radiation is collected perpendicular to the incident laser via an aspheric collection lens pair and is rotated 90° by a pair of mirrors to align the horizontal laser beam with the vertical TGS entrance slit (c.f. Fig. 10A). The MIP uses N_2 as the plasma gas which results in the spectral overlap of the rotational Raman signal of N_2 with the TS (Fig. 10B).

In order to differentiate the Raman from the TS signal, a unique polarization scheme was used to take advantage of the fact that TS is inherently polarized in the same direction as the incident laser while Raman scattering is only partially polarized. The Thomson signal can be rejected through the addition of a half-wave plate to the TGS while the rotational Raman signal is still transmitted to the iCCD (Fig. 10C). The purely Raman spectrum (Fig. 10C) is then subtracted from the overlapping signal image (Fig. 10B), after a correction factor is applied for the depolarization ratio (to minimize the remnant Raman fringes), and the resulting image containing only the Thomson signal remains (Fig. 10D). The authors make note that this polarization scheme yields

better results that are easier to obtain than traditional Raman simulation approaches. Fig. 10D shows four distinct quadrants of measured TS that are representative of the higher n_e found at the "edges" of the hollow plasma. The remaining Rayleigh signal that was not blocked by the TGS notch filter is seen by the bright vertical line in the center of the image. It is evident that the smile (curvature of the slit image) is a prominent feature of this particular TGS and is clearly asymmetric across the spatial dimension (c.f. Fig. 10B-D) thus requiring a row-by-row spectral calibration. Fig. 10D also shows two Gaussian fitted Thomson spectra taken at symmetric radial positions in the plasma torch (in relation to the axial position). The fits across multiple datasets showed a peak n_e value of about 1.3×10^{19} m^{-3} and peak T_e values of approximately 0.5 eV. The authors note that the uncertainty/variations (seen clearly in the fitted experimental data presented in Fig. 10D) arises mainly from the systematic image distortions and artifacts left after the polarization-based Raman subtraction method. Furthermore, it has been proposed that the MIP can be close to LTE when sustained in N_2 [111,112]. The authors investigated the closeness to LTE of this particular MIP by performing comparisons between experimental and modeled data. The measurement of excitations temperatures (T_{exc}) via Boltzmann plots from OES data for Cr I, Fe I, Ti I, and Ti II were used to calculate the n_e using the "Chemical Equilibrium with Applications" (CEA) model developed by NASA [113]. The T_{exc} were calculated to be ~5100 K and using the CEA model based on LTE conditions, the predicted n_e is $\sim 2 \times 10^{19}$ m^{-3} which is in good agreement with the current TS study ($n_e = 1.3 \times 10^{19}$ m^{-3}) and another experimental study performed by Ogura

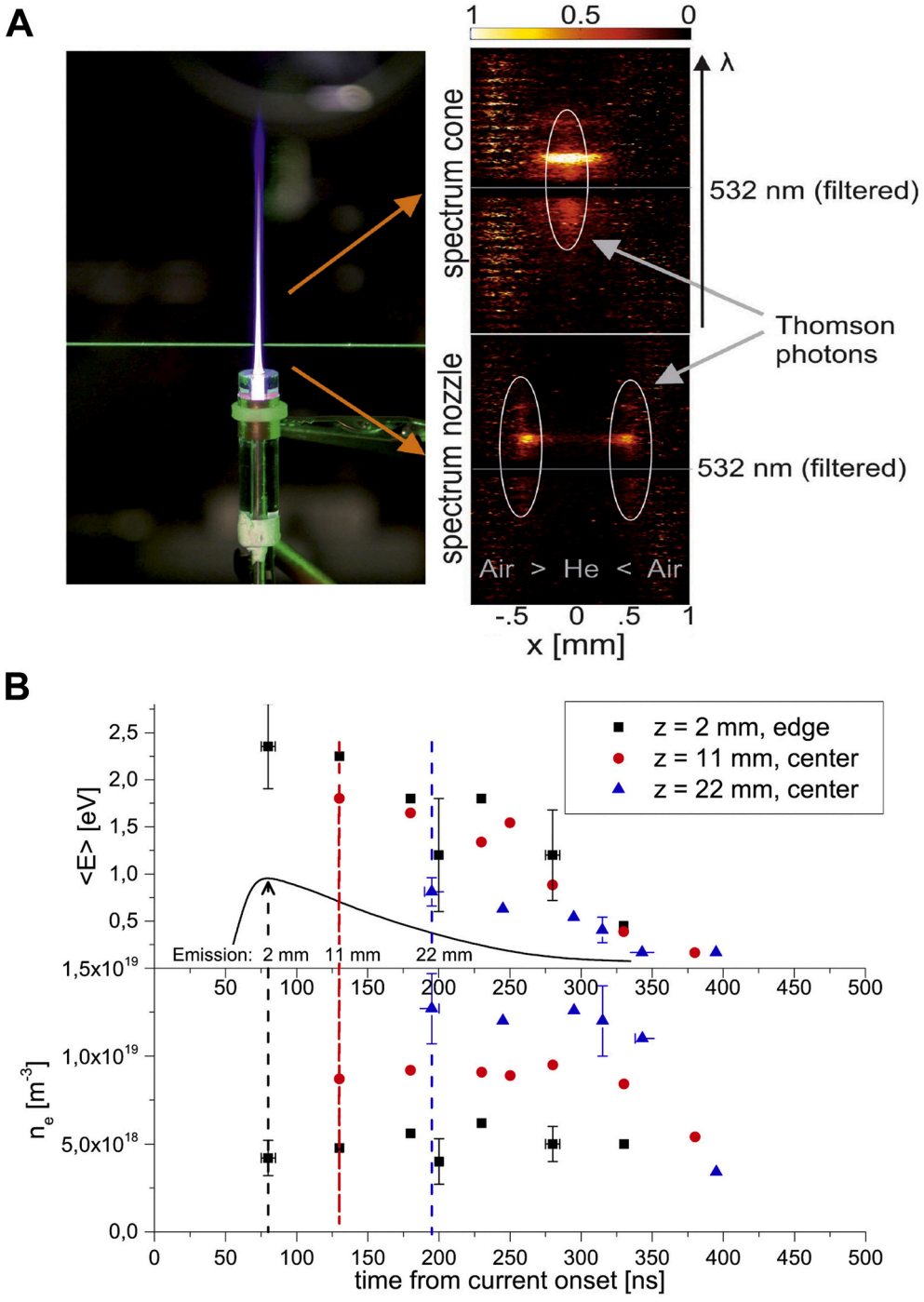

Fig. 11. (A) Photograph of the DBD atmospheric pressure plasma jet (APPJ) and the 532 nm probe laser beam. 2D TS spectra are shown at z = 11 mm (top) and z = 2 mm (bottom). The wavelength scale is roughly from 528 to 536 nm. The TS signal can be fitted to a single Gaussian distribution centered around the laser wavelength. (B) Temporal evolution of n_e and T_e at three different axial positions (z = 2 mm, 11 mm, and 22 mm) [116]. Adapted with permission from The Institute of Physics.

et al. in 1997 ($n_e = 3 \times 10^{19}$ m^{-3}) [111]. Assuming that $T_e = T_{exc}$, the previous values (derived by Boltzmann plots and CEA calculations) were substituted into the Saha-Boltzmann equation to determine the ionic-to-atomic ratio of Mg lines which showed good agreement with the experimentally measured ratios at <10% error. The n_e and T_e results from TS are in excellent agreement with those derived by T_{exc} calculations assuming LTE and the T_{exc} was shown to be almost equal to the T_e. Therefore, it can be concluded that this specific MIP torch is very close to LTE conditions and more broadly it is very likely that near LTE conditions can be predicted in MIPs operated in N_2 environments.

3.5. Atmospheric pressure plasma jets

Atmospheric pressure plasma jets (APPJs) are of growing popularity in the fields of MS and OES for chemical analysis due to their ability to ionize a variety of sample types, across a wide range of polarities and their cost-effective operation [114]. Furthermore, the use of these plasmas as ambient ionization sources for MS is of great interest because they require little-to-no sample preparation and can provide soft-ionization pathways. The production of ionizing species, such as He metastables, $(H_2O)_nH^+$, O_2^+ and NO^+, is directly related to electron reactions, thus the spatiotemporally resolved information of n_e and T_e from APPJs can provide insight into reagent species' production mechanisms. However, the recent development of novel APPJs leaves much to be understood in terms of the electron properties and how they change as a function of geometry/modality [115]. TS has been successfully used to measure the n_e and T_e distributions on pulsed He jets operated at atmospheric pressure. Given the typically low n_e of these types of plasmas, because of the low degree of ionization (10^{-4} to 10^{-7}), TGS are implemented, to minimize the much stronger Rayleigh scattering and stray light, when performing TS diagnostics.

Hübner et al. measured the electron properties (n_e and T_e) of a nanosecond-pulsed dielectric barrier discharge (DBD) APPJ with high spatial (100 μm) and temporal (2 ns) resolution via TGS TS [116]. The plasma device consists of a quartz tube with a coaxial inner capillary electrode glued inside and a 1 cm-wide grounded electrode ring wrapped around the quartz tube (Fig. 11A). With He gas flowing directly through the capillary electrode at 4.5 slpm, the plasma is generated by applying 7 kV, 250 ns duration pulses that is driven at 20 kHz to the inner capillary electrode. The authors implemented a second harmonic Nd:YAG laser at 532 nm with a repetition frequency of 5 kHz, a pulse width of 8 ns, and a pulse energy of 4 mJ that provides a laser beam with a diameter smaller than 100 μm at the plasma jet. The scattered photons are detected at a 90° collection angle by a TGS with an iCCD camera that is synchronized to the high voltage power supply and the laser pulses. The overlapped Raman scattering of N_2 and O_2 in the air with TS spectra are disentangled by calculating the Raman spectra in Matlab® using the absolute pressure and densities of N_2 and O_2, which can be obtained by fitting the Raman spectra of ambient air without plasma [41]. At 2 mm above the exit of the tube (z = 2 mm), the TS signal is detected near the edge, between the jet and the air, while at z = 11 mm the TS signal can only be detected around the radial center (Fig. 11A). It was found that the n_e along the jet axis generally evolves from hollow to axis centered, due to the higher breakdown field in the ambient air than in He, thus confining the discharge inside the jet. Furthermore, the temporal evolution shows the mean electron energy decays in time for all positions along the jet axis with the highest up to 2.5 eV at 80 ns close to the electrode (z = 2 mm) (Fig. 11B). On the other hand, the n_e varies slightly during the pulse, but drops steeply as the pulse is terminated. It should be noticed that the n_e increases along the jet axis and reaches the maximum after a propagation of several centimeters. The successive study by Douat et al. shows that the density of He (2^3S_1) metastables decays along jet propagation, if the repetition rate is less than 5 kHz, while it reaches the maximum at around 12 mm away from the DBD tube exit [117]. This maximum depends on the applied voltage if the repetition rate is higher than 5 kHz which indicates the repetition rate of the plasma pulse can significantly affect the spatial distribution of He (2^3S_1) metastables along the jet axis and in turn the n_e via Penning ionization. Furthermore, they proposed that at repetition rate higher than 5 kHz, the residual negative ions (O^-, O_2^-, OH^-, O_3^- and $H_2O_2^-$ [118]) in the He-air boundary collide with the streamer head at the following duty cycle, hence inducing electron detachment (via photo or collisional processes) and in turn results in a higher n_e. These negative ions are long-lived (some hundreds of microseconds deduced from the 5 kHz watershed) at the He-air boundary because of the slow diffusion and small positive-ion/negative-ion recombination rate at atmospheric pressure.

Jiang et al. also investigated the electron properties of a DBD atmospheric-pressure nanosecond pulsed plasma jets (APNPJs) driven at a much lower repetition rate (10 Hz) via TGS TS [119]. The Raman scattering spectrum of N_2 and O_2 is simulated in Igor Pro© assuming 78% N_2 and 21% O_2 composition of the air, in order to extract the TS signal. The discharge cell consists of a concentric tubular Cu electrode (i.d. 3.2 mm, o.d. 6.4 mm) enclosed in a ceramic cylindrical structure and the inner diameter reduces to 1 mm at the nozzle exit with a 3 mm-wide copper tape wrapped around the ceramic nozzle, which serves as the grounded electrode (Fig. 12A).

With helium gas flowing at 1 slpm, the plasma is generated by applying 9 kV, 150 ns duration pulses that are driven at 10 Hz to the inner electrode. At an axial distance z = 1 mm from the nozzle surface, the TS peak intensity is higher around the edges of the jet than the radial center (Fig. 12B), which indicates the n_e distribution is in the shape of a hollow ring with the peak density of ~9–11 × 10^{19} m^{-3} at $r = 0.3$ mm. On the other hand, the n_e reaches the detection limit of ~2.0 × 10^{19} m^{-3} within $r = 0.2$ mm, thus the error associated with the data is relatively large. The authors suggested that the ring-shape distribution of electrons is attributed to the hollow electrode geometry and the dynamics of the He gas flow. Higher ionization rates at the radial boundary are achieved due to direct electron impact ionizations of O_2 and N_2, Penning ionization of O_2 and N_2, as well as ionization of He, He metastables, and He dimers all taking place at the boundary between the jet and the air, while the electrons generated in the radial center of the jet are mostly from the ionization of He, He metastables and He dimers. Moreover, the spatiotemporal mapping of the n_e at z = 1 mm shows two peaks (80 ns and 140 ns) during the temporal development instead of decaying monotonically (Fig. 12C). The observation of the n_e peak at 140 ns is due to the jet current becoming negative and thus reigniting the discharge. The spatiotemporal mapping of the T_e at z = 1 mm shows that the T_e decreases with time (Fig. 12D). It is noteworthy to mention that there is no laser-induced fluorescence observed in this study near the laser wavelength compared with the study of Hübner et al. discussed above [116]. This difference can be contributed to the repetition rate of the high voltage pulse being much lower (i.e. 10 Hz) in this study, which results in a lower concentration of He metastables, caused by the remaining long-lived negative ions from the previous pulse. It is also worth noting that the n_e decays with the jet propagation along the axial position, which is contrary to the study of Hübner et al. [116]. This could also be because of the much lower repetition rate of the high voltage pulse inducing a much lower concentration of He metastables in the plume while the shorter pulse duration (i.e. 150 ns) reduces the propagation length of the plasma plume.

3.6. Conclusions and future directions

It is evident that TS has found a niche in diagnostics of plasmas used for chemical analysis. In addition to the inherent advantages TS has over other diagnostic techniques, novel instrumentation development and data processing methods have provided the means to accurately measure previously inaccessible electron parameters at relatively quick single measurement (1 signal and 1 background image) time scales (≤ 10 min for $n_e \sim 10^{11}$ cm^{-3} [54] and single laser shot measurements for

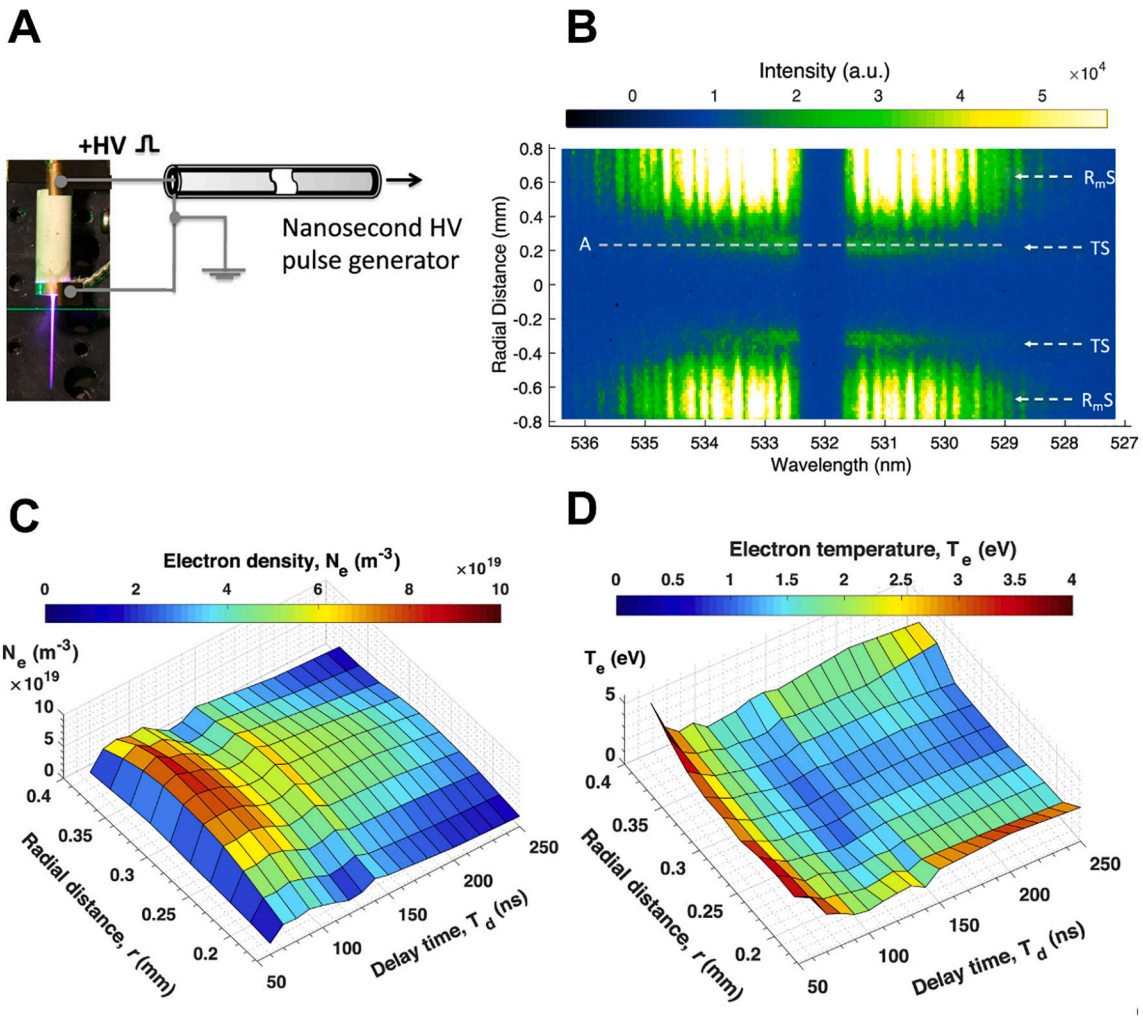

Fig. 12. (A) Image of the DBD atmospheric-pressure nanosecond pulsed plasma jet (APNPJ) with a 532 nm laser beam. (B) The 2D TS and Raman scattering spectrum at an axial distance z = 1 mm from the nozzle surface. (C) Spatiotemporal development of the n_e of the APNPJ at z = 1 mm. (D) Spatiotemporal development of the T_e of the APNPJ at z = 1 mm [119]. Adapted with permission from The Institute of Physics.

$n_e \sim 10^{15}$ cm^{-3} [120]). Lower limits-of-detection, better stray light rejection, and higher contrast have allowed access to lower density plasmas such as MIPs and GDs. Plasmas that are operated in environments where molecular species are present, such as APPJs, have been traditionally avoided due to the overlap of Raman scattering. In such cases, well-defined differentiation schemes have now become common for extraction of the Thomson scattered spectra. As of now, numerous TS studies have been performed to deepen the fundamental understanding of plasmas used for chemical analysis, but there are still many areas left to investigate.

Recently, ICP has found novel uses in single-cell and nanoparticle analysis [121], and has been coupled with micro-droplet generators for this purpose [122]. As such, fundamental studies performed under such conditions are gaining renewed interest. These include earlier studies, for example, Olesik and co-workers have characterized the changes in droplet diameter during desolvation via Mie scattering analysis [123], as well as the signal fluctuations that occur due to individual droplets, vaporizing particles, and incompletely desolvated droplets [124–127]. The work of Lazar and Farnsworth is of particular relevance here, including their investigations into matrix effects using monodisperse droplet via laser-excited atomic fluorescence spectroscopy (LEAFS) and OES [128,129]. More recent studies include one by Chan and Hieftje where they report thermal pinching in the vicinity of droplets in the ICP [130]. It would be of great interest to perform future TS studies under these single-droplet operating conditions. Such studies would give further insights into the changes in n_e and T_e during the processes of desolvation close to the droplet. Nevertheless, instrumentation with higher contrast and stray light rejection would be necessary to prevent the light scattered from the droplet from "drowning" the TS signal from the lower n_e expected in the adjacent regions.

Regarding GD, while typical GDOES operating conditions result in poor lateral resolution (mm), due to the mixing of the atoms in the discharge, it has been shown that operating the GD under pulsed-power mode and higher-pressure allows elemental mapping [4,131]. Furthermore, RF power offers the advantage of being able to analyze nonconductive samples in comparison to traditional DC GD. TS experiments need to be applied for elucidation of the underlying species behavior and mechanisms that govern the plasma-based chemical analysis, especially as a function of time along the pulse train, under these new elemental mapping conditions. The design/construction of an improved transmission-type TGS for low-density plasmas has just been published by Finch et al. which also included proof-of-principle measurements on a pulsed-power RF GD, thus allowing such future studies to be performed [54]. Another interesting area that would benefit from TS studies is the application of combined hollow cathode GDs with time-of-flight MS [132,133]. An experimental setup as proposed by Vincent et al. in 2018, would allow such a study to be performed [38].

In the area of LIP, the large discrepancies seen of electron parameters

between TS experiments, other diagnostic methods, and simulations shows that many LIP processes are not well understood and have benefited greatly from the implementation of independent TS experiments. There are many more studies that need to be performed on LIPs before a good understanding of plasma-laser-sample interactions can be realized. It would be of great interest to investigate the electron parameters very close to the sample surface during a LIBS experiment as a function of plume evolution over time, to elucidate the surface effects. Furthermore, there has been great success in using LIBS to perform elemental analysis on the Martian planet via the Curiosity rover's ChemCam instrument suite [100]. However, the electron parameters under the lower pressure and high CO_2 atmospheric conditions on Mars are not characterized well, thus leaving an area of great interest where TS needs to be applied in future studies.

With respect to MIP, the distributions of n_e and T_e have been studied spatially and shown to have drastically different values based on the MIP geometry and gas used to sustain them. The operation of MIPs in ambient air further complicates the electron parameters and TS has shown great promise for elucidating these complexities. Further 2D TS measurements would be of great value for MIPs used in chemical analysis as very few have been performed to date. Another area that would benefit greatly from TS analysis is the fundamental study of the novel microwave inductively coupled atmospheric-pressure plasma (MICAP), whose performance for chemical analysis has been studied by Hieftje et al., and recently by Günther et al., and has been shown to have great potential [110,134,135].

On the other hand, the rapid demand for novel APPJs and the maturing of these plasmas as ambient ionization sources, shows there are many TS studies that still need to be performed. Notably, low-temperature plasmas (LTP), flowing atmospheric pressure afterglow (FAPA), direct analysis in real time (DART), desorption atmospheric-pressure chemical ionization (DAPCI), and desorption ionization by charge exchange (DICE) [136], etc, would be of great interest to characterize due to their implementation for a wide variety of applications from analysis of uranium isotope ratios [137] to monitoring of volatiles in exhaled breath [9]. However, the TS signal is much weaker compared with Rayleigh scattering and Raman scattering signal due to the low n_e. Possible improvements such as implementing higher numerical aperture collection optics and using a probe laser with a longer wavelength need to be further investigated to increase the contrast for TS studies.

Declaration of Competing Interest

The authors declare that they have no known competing financial interests or personal relationships that could have appeared to influence the work reported in this paper.

Acknowledgments

The authors would like to acknowledge support by the National Science Foundation under CHE-1610849. This work was also supported in part by the Undergraduate Research Program at the Center for the Integration of STEM Education and Research and the Center for Transformative Undergraduate Experiences at Texas Tech University.

References

[1] A. Bogaerts, Plasma diagnostics and numerical simulations: insight into the heart of analytical glow discharges, J. Anal. At. Spectrom. 22 (2007) 13–40.
[2] P. Belenguer, M. Ganciu, P. Guillot, T. Nelis, Pulsed glow discharges for analytical applications, Spectrochim. Acta B At. Spectrosc. 64 (2009) 623–641.
[3] P.W.J.M. Boumans, Inductively Coupled Plasma Emission Spectroscopy Part II: Applications and Fundamentals Volume 2, John Wiley and Sons, United States, 1987.
[4] G. Gamez, M. Voronov, S. Ray, V. Hoffmann, G. Hieftje, J. Michler, Surface elemental mapping via glow discharge optical emission spectroscopy, Spectrochim. Acta B At. Spectrosc. 70 (2012) 1–9.
[5] R.K. Marcus, J.A.C. Broekaert, Glow Discharge Plasmas in Analytical Spectroscopy, John Wiley & Sons, New York, 2003.
[6] M. Wilke, G. Teichert, R. Gemma, A. Pundt, R. Kirchheim, H. Romanus, P. Schaaf, Glow discharge optical emission spectroscopy for accurate and well resolved analysis of coatings and thin films, Thin Solid Films 520 (2011) 1660–1667.
[7] L. Wilken, V. Hoffmann, K. Wetzig, In situ depth measurements for GD-OES, J. Anal. At. Spectrom. 18 (2003) 1133–1140.
[8] G. Gamez, K. Finch, Recent advances in surface elemental mapping via glow discharge atomic spectrometry, Spectrochim. Acta B At. Spectrosc. 148 (2018) 129–136.
[9] X. Gong, S. Shi, G. Gamez, Real-time quantitative analysis of Valproic acid in exhaled breath by low temperature plasma ionization mass spectrometry, J. Am. Soc. Mass Spectrom. 28 (2017) 678–687.
[10] J.J.A.M. van der Mullen, G. Boidin, M.J. van de Sande, High-resolution electron density and temperature maps of a microwave plasma torch measured with a 2-D Thomson scattering system, Spectrochim. Acta B At. Spectrosc. 59 (2004) 929–940.
[11] K. Warner, G.M. Hieftje, Thomson scattering from analytical plasmas, Spectrochim. Acta B At. Spectrosc. 57 (2002) 201–241.
[12] M.N. Saha, On a physical theory of stellar spectra, Proc. Roy. Soc. Lond. A 99 (1921) 135.
[13] M.N. Saha, Ionization in the solar chromosphere, The London, Edinburgh, and Dublin, Philos. Mag. J. Sci. 40 (1920) 472–488.
[14] S.A. Triger, A.L. Khomkin, A.S. Shumikhin, Ionization transition in low-density plasma, Plasma Phys. Rep. 37 (2011) 816.
[15] E.A.D. Carbone, S. Nijdam, Thomson scattering on non-equilibrium low density plasmas: principles, practice and challenges, Plasma Phys. Controlled Fusion 57 (2015), 014026.
[16] H. Simon, J.S. Sousa, J.J.A.M. van der Mullen, G.G. William, Thomson scattering on non-thermal atmospheric pressure plasma jets, Plasma Sources Sci. Technol. 24 (2015) 054005.
[17] M.J. van de Sande, Laser scattering on low temperature plasmas : high resolution and stray light rejection, Eindhoven University of Technology, 2002.
[18] S. Shi, X. Gong, Y. Mu, K. Finch, G. Gamez, Geometric super-resolution on push-broom hyperspectral imaging for plasma optical emission spectroscopy, J. Anal. At. Spectrom. 33 (2018) 1745–1752.
[19] S. Ries, N. Bibinov, M. Rudolph, J. Schulze, S. Mráz, J.M. Schneider, P. Awakowicz, Spatially resolved characterization of a dc magnetron plasma using optical emission spectroscopy, Plasma Sources Sci. Technol. 27 (2018), 094001.
[20] J. Licki, Analysis of the effect of the self- reversal of spectral lines on the measurement of plasma (or flame) temperature, High Temp. 8 (1970) 472–477.
[21] C. Haisch, Optical tomography, Annu. Rev. Anal. Chem. 5 (2012) 57–77.
[22] R. Álvarez, A. Rodero, M.C. Quintero, An Abel inversion method for radially resolved measurements in the axial injection torch, Spectrochim. Acta B At. Spectrosc. 57 (2002) 1665–1680.
[23] S. Shi, K. Finch, Y. She, G. Gamez, Development of Abel's inversion method to extract radially resolved optical emission maps from spectral data cubes collected via push-broom hyperspectral imaging with sub-pixel shifting sampling, J. Anal. At. Spectrom. 35 (2020) 117–125.
[24] E. Goursat, Sur un probleme d'inversion resolu par Abel, Acta Math. 27 (1903) 129–133.
[25] K. Dzierżęga, A. Mendys, B. Pokrzywka, What can we learn about laser-induced plasmas from Thomson scattering experiments, Spectrochim. Acta B At. Spectrosc. 98 (2014) 76–86.
[26] A. Bogaerts, R. Gijbels, G. Gamez, G.M. Hieftje, Fundamental studies on a planar-cathode direct current glow discharge. Part II: numerical modeling and comparison with laser scattering experiments, Spectrochim. Acta B At. Spectrosc. 59 (2004) 449–460.
[27] A. Bogaerts, A. Quentmeier, N. Jakubowski, R. Gijbels, Plasma diagnostics of an analytical Grimm-type glow discharge in argon and in neon: Langmuir probe and optical emission spectrometry measurements, Spectrochim. Acta B At. Spectrosc. 50 (1995) 1337–1349.
[28] G. Gamez, A. Bogaerts, F. Andrade, G.M. Hieftje, Fundamental studies on a planar-cathode direct current glow discharge. Part I: characterization via laser scattering techniques, Spectrochim. Acta B At. Spectrosc. 59 (2004) 435–447.
[29] G. Gamez, A. Bogaerts, G.M. Hieftje, Temporal and spatially resolved laser-scattering plasma diagnostics for the characterization of a ms-pulsed glow discharge, J. Anal. At. Spectrom. 21 (2006) 350–359.
[30] M. Kuraica, N. Konjević, M. Platiša, D. Pantelić, Plasma diagnostics of the Grimm-type glow discharge, Spectrochim. Acta B At. Spectrosc. 47 (1992) 1173–1186.
[31] Y. Ye, R.K. Marcus, Langmuir probe study of the charged particle characteristics in an analytical radio frequency-glow discharge. Roles of discharge conditions and sample conductivity, Spectrochim. Acta B At. Spectrosc. 51 (1996) 509–531.
[32] M.D. Bowden, M. Kogano, Y. Suetome, T. Hori, K. Uchino, K. Muraoka, Comparison of electron property measurements in an inductively coupled plasma made by Langmuir probe and laser Thomson scattering techniques, J. Vac. Sci. Technol. A 17 (1999) 493–499.
[33] A. Woodard, K. Shojaei, C. Berrospe-Rodriguez, G. Nava, L. Mangolini, Electron emission from particles strongly affects the electron energy distribution in dusty plasmas, J. Vac. Sci. Technol. A 38 (2020), 023005.
[34] J.-H. Kim, D.-C. Kwon, C.-W. Chung, Effect of low frequency power on the electron energy distribution function in argon inductively coupled plasmas, J. Vac. Sci. Technol. B 38 (2020), 022801.
[35] A. Scheeline, M.J. Zoellner, Thomson scattering as a diagnostic of atmospheric pressure discharges, Appl. Spectrosc. 38 (1984) 245–258.

[36] G. Gamez, M. Huang, S.A. Lehn, G.M. Hieftje, Laser-scattering instrument for fundamental studies on a glow discharge, J. Anal. At. Spectrom. 18 (2003) 680–684.
[37] M.J. van de Sande, J.J.A.M. van der Mullen, Thomson scattering on a low-pressure, inductively-coupled gas discharge lamp, J. Phys. D 35 (2002) 1381–1391.
[38] V. Benjamin, T. Sedina, M. Stéphane, M. Tiberiu, F. Jérôme, A compact new incoherent Thomson scattering diagnostic for low-temperature plasma studies, Plasma Sources Sci. Technol. 27 (2018), 055002.
[39] M. Huang, K. Warner, S. Lehn, G.M. Hieftje, A simple approach to deriving an electron energy distribution from an incoherent Thomson scattering spectrum, Spectrochim. Acta B At. Spectrosc. 55 (2000) 1397–1410.
[40] M. Huang, G.M. Hieftje, A new procedure for determination of electron temperatures and electron concentrations by Thomson scattering from analytical plasmas, Spectrochim. Acta B At. Spectrosc. 44 (1989) 291–305.
[41] A.F.H. van Gessel, E.A.D. Carbone, P.J. Bruggeman, J.J.A.M. van der Mullen, Laser scattering on an atmospheric pressure plasma jet: disentangling Rayleigh, Raman and Thomson scattering, Plasma Sources Sci. Technol. 21 (2012), 015003.
[42] H. Zhang, Y. Wu, H. Sun, F. Yang, M. Rong, F. Jiang, Investigations of laser-induced plasma in air by Thomson and Rayleigh scattering, Spectrochim. Acta B At. Spectrosc. 157 (2019) 6–11.
[43] H. Kempkens, J. Uhlenbusch, Scattering diagnostics of low-temperature plasmas (Rayleigh scattering, Thomson scattering, CARS), Plasma Sources Sci. Technol. 9 (2000) 492–506.
[44] K. Dzierżęga, W. Zawadzki, B. Pokrzywka, S. Pellerin, Experimental investigations of plasma perturbation in Thomson scattering applied to thermal plasma diagnostics, Phys. Rev. E 74 (2006), 026404.
[45] M. Sneep, W. Ubachs, Direct measurement of the Rayleigh scattering cross section in various gases, J. Quant. Spectrosc. Radiat. Transf. 92 (2005) 293–310.
[46] I.H. Hutchinson, Principles of Plasma Diagnostics, 2 ed., Cambridge University Press, Cambridge, 2002.
[47] H.R. Griem, Principles of Plasma Spectroscopy, Cambridge University Press, Cambridge, 1997.
[48] A.E. Siegman, Lasers, University Science Books, 1986.
[49] E.E. Salpeter, Electron density fluctuations in a plasma, Phys. Rev. 120 (1960) 1528–1535.
[50] A. Obrusník, P. Synek, S. Hübner, J.J.A.M. van der Mullen, L. Zajíčková, S. Nijdam, Coherent and incoherent Thomson scattering on an argon/hydrogen microwave plasma torch with transient behaviour, Plasma Sources Sci. Technol. 25 (2016), 055018.
[51] D.E. Evans, J. Katzenstein, Laser light scattering in laboratory plasmas, Rep. Prog. Phys. 32 (1969) 207–271.
[52] D.H. Froula, S.H. Glenzer, N.C. Luhmann, J. Sheffield, Chapter 4 - noncollective scattering, in: D.H. Froula, S.H. Glenzer, N.C. Luhmann, J. Sheffield (Eds.), Plasma Scattering of Electromagnetic Radiation, Second edition, Academic Press, Boston, 2011, pp. 69–102.
[53] N. Chalyavi, P.S. Doidge, R.J.S. Morrison, G.B. Partridge, Fundamental studies of an atmospheric-pressure microwave plasma sustained in nitrogen for atomic emission spectrometry, J. Anal. At. Spectrom. 32 (2017) 1988–2002.
[54] K. Finch, A. Hernandez, Y. She, S. Shi, G. Gamez, A transmission-type triple grating spectrograph for improved laser scattering diagnostics of low-density plasmas used in chemical analysis, J. Anal. At. Spectrom. 35 (2020) 1932–1946.
[55] K. Dzierżęga, W. Zawadzki, F. Sobczuk, M.L. Sankhe, S. Pellerin, M. Wartel, W. Olchawa, A. Bacławski, A. Bartecka, Experimental and theoretical studies of Stark profiles of Ar I 696.5 nm spectral line in laser-induced plasma, J. Quantit. Spectrosc. Radiat. Transfer 237 (2019) 106635.
[56] Andor, Shamrock 500i Spec. Sheet, https://andor.oxinst.com/assets/uploads/products/andor/documents/andor-shamrock-500-specifications.pdf, Accessed 6/6/2020.
[57] M.N. Shneider, Ponderomotive perturbations of low density low-temperature plasma under laser Thomson scattering diagnostics, Phys. Plasmas 24 (2017) 100701.
[58] H.J. Kunze, The Laser as a Tool for Plasma Diagnostics, North-Holland Publishing Company, 1968.
[59] A.B. Murphy, Electron heating in the measurement of electron temperature by Thomson scattering: are thermal plasmas thermal? Phys. Rev. Lett. 89 (2002) 8.
[60] A.B. Murphy, Thomson scattering diagnostics of thermal plasmas: laser heating of electrons and the existence of local thermodynamic equilibrium, Phys. Rev. E 69 (2004) 1.
[61] V.S. Burakov, Criteria for a plasma not to be affected by powerful laser beams, J. Appl. Spectrosc. 18 (1973) 444.
[62] S. Bivona, R. Daniele, G. Ferrante, Laser-assisted inverse bremsstrahlung in a weakly ionised plasma, J. Phys. B 15 (1982) 1585.
[63] E.A.D. Carbone, J.M. Palomares, S. Hübner, E. Iordanova, J.J.A.M. van der Mullen, Revision of the criterion to avoid electron heating during laser aided plasma diagnostics (LAPD), J. Instrument. 7 (2012) C01016.
[64] M.A.M. ElSabbagh, H. Koyama, M.D. Bowden, K. Uchino, K. Muraoka, A laser Thomson scattering system for low density glow discharge plasmas, Jpn. J. Appl. Phys. 40 (2001) 1465–1466.
[65] J.W. Olesik, Elemental analysis using ICP-OES and ICP/MS, Anal. Chem. 63 (1991) 12A–21A.
[66] N.N. Sesi, D.S. Hanselman, P. Galley, J. Horner, M. Huang, G.M. Hieftje, An imaging-based instrument for fundamental plasma studies, Spectrochim. Acta B At. Spectrosc. 52 (1997) 83–102.
[67] K.A. Marshall, G.M. Hieftje, Thomson scattering for determining electron concentrations and temperatures in an inductively coupled plasma-II. Description and evaluation of a multichannel instrument, Spectrochim. Acta B At. Spectrosc. 43 (1988) 851–865.
[68] K.A. Marshall, G.M. Hieftje, Thomson scattering for determining electron concentrations and temperatures in an inductively coupled plasma-I. Assessment of the technique for a low—flow, low—power plasma, Spectrochimica Acta Part B: Atomic Spectrosc. 43 (1988) 841–849.
[69] M. Huang, G.M. Hieftje, Thomson scattering from an ICP, Spectrochim. Acta B At. Spectrosc. 40 (1985) 1387–1400.
[70] J.M. de Regt, R.A.H. Engeln, F.P.J. de Groote, J.J.A.M. van der Mullen, D. C. Schram, Thomson scattering experiments on a 100 MHz inductively coupled plasma calibrated by Raman scattering, Rev. Sci. Instrum. 66 (1995) 3228–3233.
[71] J.M. de Regt, J.J.A.M. van der Mullen, D.C. Schram, Response of the electron density and temperature to the power interruption measured by Thomson scattering in an inductively coupled plasma, Phys. Rev. E 52 (1995) 2982–2987.
[72] J.J.A.M. van der Mullen, J.M. de Regt, An active spectroscopical study on the plasma parameters of an ICP, Fresenius J. Anal. Chem. 355 (1996) 532–537.
[73] E. Bolea-Fernandez, A. Rua-Ibarz, M. Velimirovic, K. Tirez, F. Vanhaecke, Detection of microplastics using inductively coupled plasma-mass spectrometry (ICP-MS) operated in single-event mode, J. Anal. At. Spectrom. 35 (2020) 455–460.
[74] G. Gamez, S.A. Lehn, M. Huang, G.M. Hieftje, Effect of mass spectrometric sampling interface on the fundamental parameters of an inductively coupled plasma as a function of its operating conditions: part II. Central-gas flow rate and sampling depth, Spectrochim. Acta B At. Spectrosc. 62 (2007) 370–377.
[75] G. Gamez, S.A. Lehn, M. Huang, G.M. Hieftje, Effect of mass spectrometric sampling interface on the fundamental parameters of an inductively coupled plasma as a function of its operating conditions: part I. Applied r.f. power and vacuum, Spectrochim. Acta B At. Spectrosc. 62 (2007) 357–369.
[76] H. Ma, N. Taylor, P.B. Farnsworth, The effect of the sampling interface on spatial distributions of barium ions and atoms in an inductively coupled plasma ion source, Spectrochim. Acta B At. Spectrosc. 64 (2009) 384–391.
[77] M. Aghaei, H. Lindner, A. Bogaerts, The effect of the sampling cone position and diameter on the gas flow dynamics in an ICP, J. Anal. At. Spectrom. 28 (2013) 1485–1492.
[78] A. Bogaerts, R. Gijbels, Fundamental aspects and applications of glow discharge spectrometric techniques, Spectrochim. Acta B At. Spectrosc. 53 (1998) 1–42.
[79] J. Angeli, A. Bengtson, A. Bogaerts, V. Hoffmann, V.-D. Hodoroaba, E. Steers, Glow discharge optical emission spectrometry: moving towards reliable thin film analysis–a short review, J. Anal. At. Spectrom. 18 (2003) 670–679.
[80] R. Escobar Galindo, R. Gago, D. Duday, C. Palacio, Towards nanometric resolution in multilayer depth profiling: a comparative study of RBS, SIMS, XPS and GDOES, Analyt. Bioanalyt. Chem. 396 (2010) 2725–2740.
[81] S. Mohajernia, A. Mazare, I. Hwang, S. Gaiaschi, P. Chapon, H. Hildebrand, P. Schmuki, Depth elemental characterization of 1D self-aligned TiO2 nanotubes using calibrated radio frequency glow discharge optical emission spectroscopy (GDOES), Appl. Surf. Sci. 442 (2018) 412–416.
[82] B. Fernández, R. Pereiro, A. Sanz-Medel, Glow discharge analysis of nanostructured materials and nanolayers—a review, Anal. Chim. Acta 679 (2010) 7–16.
[83] C.L. Lewis, L. Li, J.T. Millay, S. Downey, J. Warrick, F.L. King, Temporal emission characteristics of millisecond pulsed radiofrequency and direct current glow discharges, J. Anal. At. Spectrom. 18 (2003) 527–532.
[84] N.P. Ferreira, H.G.C. Human, L.R.P. Butler, Kinetic temperatures and electron densities in the plasma of a side view Grimm-type glow discharge, Spectrochim. Acta B At. Spectrosc. 35 (1980) 285–295.
[85] D. Fang, R.K. Marcus, Use of a cylindrical Langmuir probe for the characterization of charged particle populations in a planar, diode glow discharge device, Spectrochim. Acta B At. Spectrosc. 45 (1990) 1053–1074.
[86] M. Numano, O. Furukawa, I. Michiyoshi, Comparison of Langmuir probe and spectroscopic electron temperature measurements, Plasma Physics 13 (1971) 992–995.
[87] W.K. McGregor, L.E. Brewer, Equivalence of Electron and Excitation Temperatures in an Argon Plasma, Phys. Fluids 9 (1966) 826.
[88] H. Park, S.J. You, W. Choe, Correlation between excitation temperature and electron temperature with two groups of electron energy distributions, Phys. Plasmas 17 (2010) 103501.
[89] S.K. Ohorodnik, W.W. Harrison, Plasma diagnostic measurements in the cryogenically cooled glow discharge, J. Anal. At. Spectrom. 9 (1994) 991–996.
[90] D. Fang, R.K. Marcus, Effect of discharge conditions and cathode identity on charged particle populations in the negative glow region of a simple diode glow discharge, Spectrochim. Acta B At. Spectrosc. 46 (1991) 983–1000.
[91] C.D. West, H.G.C. Human, Self-absorption and Doppler temperatures of emission lines excited in a glow discharge lamp, Spectrochim. Acta B At. Spectrosc. 31 (1976) 81–92.
[92] A. Bogaerts, R. Gijbels, V.V. Serikov, Calculation of gas heating in direct current argon glow discharges, J. Appl. Phys. 87 (2000) 8334–8344.
[93] W.W. Harrison, Pulsed glow discharge as a solids analysis source, J. Anal. At. Spectrom. 13 (1998) 1051–1056.
[94] W.W. Harrison, W.E.I. Hang, X. Yan, K. Ingeneri, C. Schilling, Temporal considerations with a microsecond pulsed glow discharge, J. Anal. At. Spectrom. 12 (1997) 891–896.
[95] A. Bogaerts, R. Gijbels, G.P. Jackson, Modeling of a millisecond pulsed glow discharge: investigation of the afterpeak, J. Anal. At. Spectrom. 18 (2003) 533–548.

[96] A. Bogaerts, The afterglow mystery of pulsed glow discharges and the role of dissociative electron–ion recombination, J. Anal. At. Spectrom. 22 (2007) 502–512.
[97] B. Busser, S. Moncayo, J.L. Coll, L. Sancey, V. Motto-Ros, Elemental imaging using laser-induced breakdown spectroscopy: a new and promising approach for biological and medical applications, Coord. Chem. Rev. 358 (2018) 70–79.
[98] J.R. Chirinos, D.D. Oropeza, J.J. Gonzalez, H. Hou, M. Morey, V. Zorba, R. E. Russo, Simultaneous 3-dimensional elemental imaging with LIBS and LA-ICP-MS, J. Anal. At. Spectrom. 29 (2014) 1292–1298.
[99] M. Bonta, J.J. Gonzalez, C. Derrick Quarles, R.E. Russo, B. Hegedus, A. Limbeck, Elemental mapping of biological samples by the combined use of LIBS and LA-ICP-MS, J. Anal. At. Spectrom. 31 (2016) 252–258.
[100] R.C. Wiens, S. Maurice, B. Barraclough, M. Saccoccio, W.C. Barkley, J.F. Bell, S. Bender, J. Bernardin, D. Blaney, J. Blank, M. Bouyé, N. Bridges, N. Bultman, P. Caïs, R.C. Clanton, B. Clark, S. Clegg, A. Cousin, D. Cremers, A. Cros, L. DeFlores, D. Delapp, R. Dingler, C. D'Uston, M. Darby Dyar, T. Elliott, D. Enemark, C. Fabre, M. Flores, O. Forni, O. Gasnault, T. Hale, C. Hays, K. Herkenhoff, E. Kan, L. Kirkland, D. Kouach, D. Landis, Y. Langevin, N. Lanza, F. LaRocca, J. Lasue, J. Latino, D. Limonadi, C. Lindensmith, C. Little, N. Mangold, G. Manhes, P. Mauchien, C. McKay, E. Miller, J. Mooney, R. V. Morris, L. Morrison, T. Nelson, H. Newsom, A. Ollila, M. Ott, L. Pares, R. Perez, F. Poitrasson, C. Provost, J.W. Reiter, T. Roberts, F. Romero, V. Sautter, S. Salazar, J.J. Simmonds, R. Stiglich, S. Storms, N. Striebig, J.-J. Thocaven, T. Trujillo, M. Ulibarri, D. Vaniman, N. Warner, R. Waterbury, R. Whitaker, J. Witt, B. Wong-Swanson, The ChemCam Instrument Suite on the Mars Science Laboratory (MSL) Rover: Body Unit and Combined System Tests, Space Sci. Rev. 170 (2012) 167–227.
[101] A. Mendys, K. Dzierżęga, M. Grabiec, S. Pellerin, B. Pokrzywka, G. Travaillé, B. Bousquet, Investigations of laser-induced plasma in argon by Thomson scattering, Spectrochim. Acta B At. Spectrosc. 66 (2011) 691–697.
[102] C.H. Popenoe, J.B. Shumaker Jr., Arc measurement of some argon transition probabilities, J. Res. Natl. Bur. Stand. A Phys. Chem. 69A (1965) 495–509.
[103] E. Nedanovska, G. Nersisyan, T.J. Morgan, L. Hüwel, T. Murakami, C.L.S. Lewis, D. Riley, W.G. Graham, Investigating the dynamics of laser induced sparks in atmospheric helium using Rayleigh and Thomson scattering, J. Appl. Phys. 117 (2015), 013302.
[104] M. Longenecker, L. Hüwel, L. Cadwell, D. Nassif, Laser-generated spark morphology and temperature records from emission and Rayleigh scattering studies, Appl. Opt. 42 (2003) 990–996.
[105] D. Nassif, L. Hüwel, Appearance of toroidal structure in dissipating laser-generated sparks, J. Appl. Phys. 87 (2000) 2127–2130.
[106] S. Ghosh, K. Mahesh, Numerical Simulation of Laser Induced Breakdown in Air, in: 46th AIAA Aerospace Sciences Meeting and Exhibit, American Institute of Aeronautics and Astronautics, 2008.
[107] R.P. Drake, High-Energy-Density Physics, Springer-Verlag, Berlin, 2006.
[108] M. Cvejić, M.R. Gavrilović, S. Jovićević, N. Konjević, Stark broadening of mg I and mg II spectral lines and Debye shielding effect in laser induced plasma, Spectrochim. Acta B At. Spectrosc. 85 (2013) 20–33.
[109] M.A. Gigosos, V. Cardeñoso, New plasma diagnosis tables of hydrogen stark broadening including ion dynamics, J. Phys. B Atomic Mol. Phys. 29 (1996) 4795–4838.
[110] M. Schild, A. Gundlach-Graham, A. Menon, J. Jevtic, V. Pikelja, M. Tanner, B. Hattendorf, D. Günther, Replacing the argon ICP: nitrogen microwave inductively coupled atmospheric-pressure plasma (MICAP) for mass spectrometry, Anal. Chem. 90 (2018) 13443–13450.
[111] K. Ogura, H. Yamada, Y. Sato, Y. Okamoto, Excitation temperature in high-power nitrogen microwave-induced plasma at atmospheric pressure, Appl. Spectrosc. 51 (1997) 1496–1499.
[112] D.A. Goncalves, T. McSweeney, G.L. Donati, Characteristics of a resonant iris microwave-induced nitrogen plasma, J. Anal. At. Spectrom. 31 (2016) 1097–1104.
[113] CEA (Chemical Equilibrium with Applications), downloadable program at, https://www.grc.nasa.gov/WWW/CEAWeb/ceaHome.htm.
[114] M.E. Monge, G.A. Harris, P. Dwivedi, F.M. Fernandez, Mass spectrometry: recent advances in direct open air surface sampling/ionization, Chem. Rev. 113 (2013) 2269–2308.
[115] S. Hübner, J.S. Sousa, J.J.A.M. van der Mullen, W.G. Graham, Thomson Scattering on Non-thermal Atmospheric Pressure Plasma Jets, Plasma Sources Sci. Technol. 24 (5) (2015) 054005.
[116] S. Hübner, J.S. Sousa, V. Puech, G.M.W. Kroesen, N. Sadeghi, Electron Properties in an Atmospheric Helium Plasma Jet Determined by Thomson Scattering, J. Phys. D 47 (43) (2014) 432001.
[117] C. Douat, I. Kacem, N. Sadeghi, G. Bauville, M. Fleury, V. Puech, Space-Time Resolved Density of Helium Metastable Atoms in a Nanosecond Pulsed Plasma Jet: Influence of High Voltage and Pulse Frequency, J. Phys. D 49 (28) (2016) 285204.
[118] S. Große-Kreul, S. Hübner, S. Schneider, D. Ellerweg, A. von Keudell, S. Matejčík, J. Benedikt, Mass spectrometry of atmospheric pressure plasmas, Plasma Sources Sci. Technol. 24 (2015), 044008.
[119] C. Jiang, J. Miles, J. Hornef, C. Carter, S. Adams, Electron Densities and Temperatures of an Atmospheric-Pressure Nanosecond Pulsed Helium Plasma Jet in Air, Plasma Sources Sci. Technol. 28 (8) (2019) 085009.
[120] J.J.A.M. van der Mullen, M.J. van de Sande, N. de Vries, B. Broks, E. Iordanova, A. Gamero, J. Torres, A. Sola, Single-shot Thomson scattering on argon plasmas created by the microwave plasma torch; evidence for a new plasma class, Spectrochim. Acta B At. Spectrosc. 62 (2007) 1135–1146.
[121] S.-i. Miyashita, S.-i. Fujii, K. Shigeta, K. Inagaki, Single cell analysis by using ICP-MS, in: Y. Ogra, T. Hirata (Eds.), Metallomics: Recent Analytical Techniques and Applications, Springer Japan, Tokyo, 2017, pp. 107–124.
[122] K. Shigeta, H. Traub, U. Panne, A. Okino, L. Rottmann, N. Jakubowski, Application of a micro-droplet generator for an ICP-sector field mass spectrometer – optimization and analytical characterization, J. Anal. At. Spectrom. 28 (2013) 646–656.
[123] J.W. Olesik, J.A. Kinzer, Measurement of monodisperse droplet desolvation in an inductively coupled plasma using droplet size dependent peaks in Mie scattering intensity, Spectrochim. Acta B At. Spectrosc. 61 (2006) 696–704.
[124] J.W. Olesik, J.C. Fister, Incompletely desolvated droplets in argon inductively coupled plasmas: their number, original size and effect on emission intensities, Spectrochim. Acta B At. Spectrosc. 46 (1991) 851–868.
[125] S.E. Hobbs, J.W. Olesik, Inductively coupled plasma mass spectrometry signal fluctuations due to individual aerosol droplets and vaporizing particles, Anal. Chem. 64 (1992) 274–283.
[126] J.C. Fister, J.W. Olesik, Vertical and radial emission profiles and ion-atom intensity ratios in inductively coupled plasmas: the connection to vaporizing droplets, Spectrochim. Acta B At. Spectrosc. 46 (1991) 869–883.
[127] J.W. Olesik, L.J. Smith, E.J. Williamsen, Signal fluctuations due to individual droplets in inductively coupled plasma atomic emission spectrometry, Anal. Chem. 61 (1989) 2002–2008.
[128] A.C. Lazar, P.B. Farnsworth, Matrix Effect Studies in the Inductively Coupled Plasma with Monodisperse Droplets. Part II: The Influence of Matrix on Spatially Integrated Ion Density, Appl. Spectrosc. 53 (1999) 465–470.
[129] A.C. Lazar, P.B. Farnsworth, Matrix Effect Studies in the Inductively Coupled Plasma with Monodisperse Droplets. Part I: The Influence of Matrix on the Vertical Analyte Emission Profile, Appl. Spectrosc. 53 (1999) 457–464.
[130] G.C.Y. Chan, G.M. Hieftje, Local cooling, plasma reheating and thermal pinching induced by single aerosol droplets injected into an inductively coupled plasma, Spectrochim. Acta B At. Spectrosc. 121 (2016) 55–66.
[131] G. Gamez, S.J. Ray, F.J. Andrade, M.R. Webb, G.M. Hieftje, Development of a pulsed radio frequency glow discharge for three-dimensional elemental surface imaging. 1. Application to biopolymer analysis, Anal. Chem. 79 (2007) 1317–1326.
[132] S. Potapov, E. Izrailov, V. Vergizova, M. Voronov, S. Suprunovich, M. Slyadnev, A. Ganeev, Pulsed glow discharge in thin-walled metallic hollow cathode. Analytical possibilities in atomic and mass spectrometry, J. Anal. At. Spectrom. 18 (2003) 564–571.
[133] A.A. Ganeev, M.A. Kuz'menkov, V.A. Lyubimtsev, S.V. Potapov, A.I. Drobyshev, S.S. Potemin, M.V. Voronov, Pulsed discharge in a hollow cathode with the detection of ions in a time-of-flight mass spectrometer: analytical capabilities in the analysis of solid samples, J. Anal. Chem. 62 (2007) 444–453.
[134] K.M. Thaler, A.J. Schwartz, C. Haisch, R. Niessner, G.M. Hieftje, Preliminary survey of matrix effects in the microwave-sustained, inductively coupled atmospheric-pressure plasma (MICAP), Talanta 180 (2018) 25–31.
[135] A.J. Schwartz, Y. Cheung, J. Jevtic, V. Pikelja, A. Menon, S.J. Ray, G.M. Hieftje, New inductively coupled plasma for atomic spectrometry: the microwave-sustained, inductively coupled, atmospheric-pressure plasma (MICAP), J. Anal. At. Spectrom. 31 (2016) 440–449.
[136] A.R. Venter, K.A. Douglass, J.T. Shelley, G. Hasman, E. Honarvar, Mechanisms of real-time, Proximal Sample Processing during Ambient Ionization Mass Spectrometry, Anal. Chem. 86 (2014) 233–249.
[137] T.P. Forbes, C. Szakal, Considerations for uranium isotope ratio analysis by atmospheric pressure ionization mass spectrometry, Analyst 144 (2019) 317–323.